Date of publication xxxx 00, 0000, date of current version June 28, 2021.

Digital Object Identifier 10.1109/ACCESS.2020.DOI

Trajectory-Free Control of Lower-Limb Exoskeletons Through Underactuated Total Energy Shaping

GE LV[1], (Member, IEEE), JIANPING LIN[2], (Student Member, IEEE), and ROBERT D. GREGG[2], (Senior Member, IEEE)

[1]Departments of Mechanical Engineering and Bioengineering, Clemson University, Clemson, SC 2634, USA
[2]Department of Electrical Engineering and Computer Science, Robotics Institute, University of Michigan, Ann Arbor, MI 48109, USA

Corresponding author: Robert D. Gregg (e-mail: rdgregg@umich.edu).

This work was supported by the National Science Foundation under Award CMMI-1652514/1949869. R. D. Gregg holds a Career Award at the Scientific Interface from the Burroughs Wellcome Fund.

ABSTRACT Kinematic control approaches for exoskeletons replicate normative joint kinematics associated with one specific task and user at a time, which makes it difficult to adjust to continuously-varying activities during gait training. These approaches also overly constrain individuals who have partial or full volitional control of their limbs, preventing these individuals from choosing their own preferred gait patterns. To address these issues, we proposed a matching framework for underactuated total energy shaping (i.e., shaping both the potential and kinetic energies) with human and environmental interaction to provide task-invariant, energetic assistance. In our prior work, we designed assistive strategies to compensate for lower-limb inertia in the actuated part of the mass matrix while leaving mass related terms unshaped. While these strategies have demonstrated potential gait benefits, shaping mass related terms in addition to lower-limb inertia can produce greater benefits as they are more dominant in determining human dynamics during locomotion. Moreover, previous definitions of closed-loop mass matrix with reduced inertial parameters cannot guarantee its positive definiteness. Having a non-positive definite mass matrix in the closed loop can render chaotic behaviors such as unbounded exoskeleton torques that cause danger to human users. In this paper, we generalize our prior work to shape all inertial terms in the actuated part of the mass matrix while ensuring its positive definiteness in the closed loop. In addition, given a positive-definite, closed-loop mass matrix, we prove passivity from human input to joint velocity and highlight two Lyapunov stability results based on common assumptions of human joint control policies. We then show benefits of the proposed approach and its advantages over conventional exoskeleton control methods with simulations on a human-like model. We also show that the corresponding assistive torques closely match the human torques of an able-bodied subject.

INDEX TERMS Total energy shaping, exoskeletons, rehabilitation robotics, biped locomotion

I. INTRODUCTION

Powered lower-limb exoskeletons are external mechanical structures equipped with actuators that support and assist human users during locomotion. To assist individuals with neurological conditions, such as stroke or spinal cord injury, these exoskeletons are often controlled to track predefined kinematic patterns. For instance, the powered hip-knee exoskeletons ReWalk [1], Ekso Bionics [2], and ATLAS [3] enforce pre-determined joint kinematics through a finite-state-machine structure. The control strategies of other exoskeletons, such as the Hybrid Assistive Limb [4] and the Indego exoskeleton [5], also fall into the category of trajectory tracking. Despite the fact that these exoskeletons have shown promising results in gait rehabilitation, critical barriers still exist in the control technology, which limits their overall adaptability. These kinematic control methods replicate the normative joint kinematics associated with one specific task and user at a time [6], which prohibits them from adjusting to continuously varying locomotor tasks or changes in user behavior during gait rehabilitation. Being confined to fixed gait patterns gives the user less freedom because little

or no contribution from the human user is allowed. While this may be viable for individuals who cannot volitionally control their lower-limbs, individuals with at least some volitional control ability should be allowed to make mistakes or corrections during gait training to facilitate active user learning. Moreover, switching between different reference trajectories requires accurate task recognition, which is currently difficult to achieve in practice [6]. The associated parameter tuning for multiple controllers requires even more time for different individuals [7]. A paradigm shift from task-specific, kinematic control approaches to task-invariant, energetic control approaches is needed for exoskeleton control design.

Various assistive controllers have been proposed for exoskeletons to amplify and augment human motion [8]–[10] or compensate for exoskeleton mass/inertia [11], [12]. In particular, energy-related methods have been adopted to facilitate both the control and mechanical design for exoskeletons. For instance, [13] proposes a potential energy modulation paradigm for upper-limb exoskeletons to eliminate user oscillation while accomplishing certain pre-defined tasks. In [14], the authors proposed the design of an elastic device to offload muscle forces by storing and releasing mechanical energy during stance phase. Similarly, the passive hip exoskeleton presented in [15] reduces the user's metabolic cost during running by using torsional springs to aid hip extension. While these devices are promising, they can only store and release mechanical energy injected by human users due to their passive nature in design. In other words, they are not capable of generating additional energy to assist human locomotion, which is often required and emphasized in gait rehabilitation. An energetic control method is in demand to actively alter the user's energy via powered exoskeletons for allowing greater freedom and flexibility during gait training.

Energy shaping is a control method that controls the system's energy to a specific analytical function of the system state in order to induce different dynamics via the Euler-Lagrange equations [16]. Energy shaping has been applied to bipedal locomotion to create natural, efficient gaits based on passive dynamics [17], regulate a biped's walking speed [18], and facilitate 3D walking gaits via control reduction [19]. However, prior work has been limited to simple point-foot biped models that ignore the changing contact conditions in human walking. These changing contact conditions result in different degrees of underactuation, which present significant challenges in systematically solving the matching conditions. The matching conditions are sets of nonlinear partial differential equations governing the achievable forms of a system's closed-loop energy. While these equations can be trivially solved with the case of full actuation, i.e., the number of actuators is equal to the number of degrees of freedom (DOFs), the solutions can be quite challenging to obtain for underactuated systems, i.e., the number of actuators is less than the number of DOFs. Different approaches have been proposed to simplify the solving of matching conditions. However, they either rely on assumptions, e.g., the shape variables being cyclic in the mass matrix [20], the inertia matrix and potential energy only depend on the actuated coordinates [21], or they have only been applied to simple models such as the pendulum-cart system [22] and the Acrobot system [23]. These limitations prevent the existing simplification methods from being applied to complex human-exoskeleton dynamics, which often include many DOFs and the associated mass matrix is dependent on shape variables in general. A matching paradigm for energy shaping that incorporates human-environmental interaction and eases the solving of matching conditions is needed to determine the shapeable dynamics of complex human-exoskeleton systems.

In our prior work [24], we focused on an energetic control approach that shapes the potential energy of the human body and exoskeleton in closed loop. By shaping potential energy, torques can be generated to counteract gravity. This control action yields the so-called body-weight support (BWS), which offloads the perceived weight of the user's lower extremities and center of mass. However, shaping the potential energy cannot provide the subject with direct assistance in the direction of ambulation. We therefore generalized the potential energy matching framework to the case of total energy shaping, i.e., shaping both the kinetic and potential energies of the human-exoskeleton system [25]. In particular, we chose to compensate for lower-limb inertia in the actuated part of the mass matrix. While simulation results with these strategies have indicated possible clinical benefits, the mass terms inside the shapeable part of the mass matrix remain unshaped. Compensating for the mass terms in addition to the lower-limb inertia can render greater dynamical changes to further assist human subjects. In addition, the strategies proposed in [25] cannot ensure positive definiteness of the closed-loop mass matrix. This prohibits us from establishing passivity or stability properties of the human-exoskeleton system in the closed loop. The mass terms must therefore be shaped in order to provide greater assistance while maintaining the positive definiteness of the closed-loop mass matrix.

STATEMENT OF CONTRIBUTIONS

The specific contributions of this paper can be summarized from the following four aspects: 1) Without making assumptions on the human input mapping matrix, we prove that the matching condition for human inputs are automatically satisfied as a consequence of shaping the bottom-right part of the mass matrix; 2) We generalize our prior work in [25] to shape all inertial terms in the shapeable part of the mass matrix while ensuring its positive definiteness in the closed loop; 3) Given a positive-definite, closed-loop mass matrix, we show input-output passivity from human inputs to joint velocity with total closed-loop energy as the storage function. Using common assumptions of human joint control policies, we show Lyapunov stability of the closed-loop human-exoskeleton system; 4) We show extensive results of the proposed assistive strategies such as reduced metabolic cost and human torques in simulation. We also show that exoskeleton torques that correspond to the assistive strategies closely match the human torques of an able-bodied subject.

The rest of the paper is organized as follows. In Section II, we first review the coupled human-exoskeleton dynamics. We then review the generalized matching framework for total energy shaping in Section III, after which we highlight passivity and Lyapunov stability results based on common human control policies in Section IV. In Section V, we present simulation results of the proposed energy shaping strategies and their advantages over conventional control paradigms on an human-like biped model. We also show exoskeleton torques based on an able-bodied subject's kinematic data. Finally, we summarize limitations of the proposed study and provide possible future research directions.

II. MODELING AND DYNAMICS OF THE BIPED

In this paper, we are interested in proposing a general matching framework applicable for lower-limb exoskeletons. To begin, we review the sagittal biped model and its dynamics as presented in [25]. Because walking is primarily a sagittal-plane task [26], and assisting hip flexion renders the most metabolic cost reduction [27], we therefore combine the biped's two hip joints into one for creating a model that ambulates in the sagittal plane. We also assume the upper-body mass of the biped is lumped at the hip joint for simplicity.

A. BIPED CONFIGURATION AND DYNAMICS

The biped is modeled as a kinematic chain with respect to an inertial reference frame (IRF, to be specified later) shown in Fig. 1. Depending on whether the exoskeleton is unilateral or bilateral, we choose to model the stance and swing legs separately (unilateral case [24]) or the entire lower body as a kinematic chain from the stance foot to the swing foot (bilateral case [25]). The biped's equation of motion (EOM) with contact constraints can be expressed as

$$M(q)\ddot{q} + C(q,\dot{q})\dot{q} + N(q) + A(q)^T\lambda = \tau, \qquad (1)$$

where n is the number of DOFs, $M(q) \in \mathbb{R}^{n\times n}$ is the positive-definite mass matrix, $C(q,\dot{q}) \in \mathbb{R}^{n\times n}$ is the Coriolis/centrifugal matrix, and $N(q) \in \mathbb{R}^{n\times 1}$ is the gravitational forces vector. The configuration space is given as $\mathcal{Q} = \mathbb{R}^2 \times \mathbb{T}^{n-2}$, and the corresponding configuration vector is $q = (\theta_{\mathrm{x}}, \theta_{\mathrm{y}}, \theta_{\mathrm{ab}}, q_{\mathrm{s}}^T)^T \in \mathbb{R}^n$, where $\mathbb{T}^{n-2}$ is the $(n-2)$ torus, θ_{x} and θ_{y} are the Cartesian coordinates with respect to the IRF, and $\theta_{\mathrm{ab}} \in \mathbb{S}^1$ is an absolute angle defined with respect to the vertical axis. The shape vector $q_{\mathrm{s}} \in \mathbb{R}^{n-3}$ contains joint angles based on the biped model (to be specified in the simulation section). The matrix $A(q)^T \in \mathbb{R}^{n\times c}$ is the constraint matrix defined as the gradient of the holonomic constraint functions, and c is the number of contact constraints that change during different contact conditions. The Lagrange multiplier λ is calculated using the method in [28] as

$$\begin{aligned}
&\lambda = \hat{\lambda} + \bar{\lambda}\tau, \text{where} \qquad (2)\\
&\hat{\lambda} = W(q)[\dot{A}(q)\dot{q} - A(q)M(q)^{-1}(C(q,\dot{q})\dot{q} + N(q))],\\
&\bar{\lambda} = W(q)A(q)M(q)^{-1}, \text{where}\\
&W(q) = (A(q)M(q)^{-1}A(q)^T)^{-1}.
\end{aligned}$$

Because we are modeling the human body and the exoskeleton as a whole, the torque $\tau = \tau_{\mathrm{hum}} + \tau_{\mathrm{exo}}$ at the right-hand side of (1) comprises both the human and the exoskeleton input terms, $\tau_{\mathrm{hum}} = B(q)v + J(q)^T F$ and $\tau_{\mathrm{exo}} = B(q)u$, respectively. The mapping matrix $B(q) \in \mathbb{R}^{n\times p}$ maps both the human muscle input term $v \in \mathbb{R}^p$ and the exoskeleton actuator torques $u \in \mathbb{R}^p$ into the dynamics. Without loss of generality, we assume $B(q)$ takes the form of $[0_{p\times(n-p)},\ I_p]^T$. In general, the vector F includes the interaction forces between the modeled subsystem and the connected un-modeled links. For the biped model shown in Fig. 1, the body *Jacobian* matrix $J(q)^T \in \mathbb{R}^{n\times 3}$ maps the vector $F = (F_{\mathrm{x}}, F_{\mathrm{y}}, M_{\mathrm{z}})^T \in \mathbb{R}^{3\times 1}$ in τ_{hum} into the dynamics, where F denotes the interaction forces between the hip of the stance model and the swing thigh, $(F_{\mathrm{x}}, F_{\mathrm{y}})^T$ indicates two linear forces, and M_{z} indicates a moment in the sagittal plane.

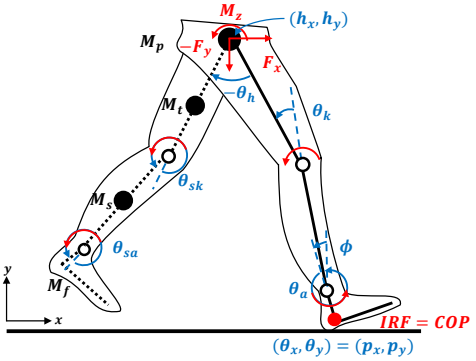

FIGURE 1. Kinematic model of the human body and the exoskeleton. The stance leg is shown in solid black and the swing leg in dashed black. The Center of Pressure (COP) is fixed at the heel as shown here during the heel contact phase. For modeling a human wearing a bilateral exoskeleton, we combine the stance and swing leg models, and the forces $(F_{\mathrm{x}}, F_{\mathrm{y}})$ are implicitly modeled in the EOM of the kinematic chain. Red arcs indicate human joint torques. For this biped model, $(\mathrm{p_x}, \mathrm{p_y})$ indicates the position of the heel, Φ denotes the angle of the heel defined with respect to the vertical axis, θ_a is the ankle angle, θ_k is the knee angle, $(\mathrm{h_x}, \mathrm{h_y})$ denotes the hip position, θ_{h} is the hip angle defined between stance and swing thighs, and θ_{sk} and θ_{sa} denote the swing knee and ankle angles, respectively.

B. HOLONOMIC CONTACT CONSTRAINTS

In the previous section, we explicitly modeled contact in the dynamics without specifying the choice of contact constraints. In this section, we define the general form of *holonomic contact constraints* encountered during the single-support period of human walking. These constraints can be expressed as relations between the position variables, i.e.,

$$a(q_1, q_2, ..., q_c) = 0_{c\times 1}, \qquad (3)$$

where q_i denotes the i-th element of the configuration vector q. The single-support period can be separated into heel contact, flat foot, and toe contact phases as in Fig. 2. Based on the contact conditions depicted in this figure, there are $c = 2$ constraints for heel contact and toe contact, whereas flat foot has $c = 3$. We will later show that the proposed framework is able to accommodate arbitrary numbers of contact constraints.

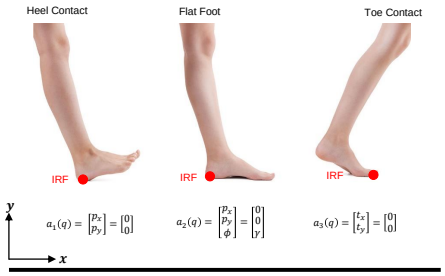

FIGURE 2. Heel contact (left), flat foot (center), and toe contact conditions (right) during the single-support period of human locomotion. To simulate dynamic walking we assume the biped is walking on a slope with angle γ, i.e., $\phi = \gamma$ during flat foot condition. The IRF is defined at the toe during toe contact with (t_x, t_y) indicating the Cartesian coordinates of the toe. This figure is reproduced from [25].

In this paper, we assume the constraint matrix $A(q)$ has the constant form

$$A(q) = \nabla_q a(q_1, q_2, q_3, ..., q_c) = [I_c \quad 0_{c\times(n-c)}]. \tag{4}$$

This constant form (i.e., $\dot{A}(q) = 0$) can be achieved by defining the IRF at the stance toe during toe contact and at the stance heel during heel and flat foot contact. Note that for the swing leg there are no contact constraints defined ($A(q) = 0$).

III. ENERGY SHAPING CONTROL

Energy shaping is a control method that alters the dynamical characteristics of a mechanical system [16]. In this section we first review the traditional definition of energy shaping and then derive the proposed matching framework.

A. ENERGY SHAPING: A BRIEF REVIEW

This section first reviews the definition for energy shaping as presented in [25]. Consider a forced n-dimensional Euler-Lagrange system with configuration space $\mathcal{Q}$ (assume $\mathbb{R}^n$ for simplicity) and its tangent bundle $T\mathcal{Q} = \bigcup_{q\in\mathcal{Q}} T_q\mathcal{Q}$. We can describe the system by a Lagrangian $\mathcal{L}(q, \dot{q})$ defined as

$$\mathcal{L}(q, \dot{q}) = \mathcal{T}(q, \dot{q}) - \mathcal{V}(q) = \frac{1}{2}\dot{q}^T M(q)\dot{q} - \mathcal{V}(q), \tag{5}$$

where the Lagrangian $\mathcal{L}(q, \dot{q}) : T\mathcal{Q} \to \mathbb{R}$ is a smooth function, $q \in \mathcal{Q}$ is the generalized coordinates vector, and $\dot{q} \in T_q\mathcal{Q}$ is the velocity vector. The scalar function $\mathcal{T}(q, \dot{q}) : T\mathcal{Q} \to \mathbb{R}$ is the kinetic energy defined based on the positive-definite mass matrix $M(q) \in \mathbb{R}^{n\times n}$, and $\mathcal{V}(q) : \mathcal{Q} \to \mathbb{R}$ is the potential energy. The Lagrangian dynamics are given by

$$\begin{aligned} &\frac{\mathrm{d}}{\mathrm{dt}}\partial_{\dot{q}}\mathcal{L}(q, \dot{q}) - \partial_q\mathcal{L}(q, \dot{q}) = \tau, \\ \Leftrightarrow\ &M(q)\ddot{q} + C(q, \dot{q})\dot{q} + N(q) = \tau, \end{aligned} \tag{6}$$

where the dynamic terms are defined similar to the ones in (1). For the underactuated case, $\tau = B(q)u$ where matrix $B(q) \in \mathbb{R}^{n\times p}$ maps the control input $u \in \mathbb{R}^p$ to the n-dimensional dynamics ($n > p$).

Now consider an unforced Euler-Lagrange system defined by another Lagrangian $\tilde{\mathcal{L}}(q, \dot{q}) : T\mathcal{Q} \to \mathbb{R}$ described as

$$\tilde{\mathcal{L}}(q, \dot{q}) = \tilde{\mathcal{T}}(q, \dot{q}) - \tilde{\mathcal{V}}(q) = \frac{1}{2}\dot{q}^T \tilde{M}(q)\dot{q} - \tilde{\mathcal{V}}(q) \tag{7}$$

with a new kinetic energy $\tilde{\mathcal{T}}(q, \dot{q}) : T\mathcal{Q} \to \mathbb{R}$ and a new potential energy $\tilde{\mathcal{V}}(q) : \mathcal{Q} \to \mathbb{R}$. The resulting Lagrangian dynamics can be expressed as

$$\begin{aligned} &\frac{\mathrm{d}}{\mathrm{dt}}\partial_{\dot{q}}\tilde{\mathcal{L}}(q, \dot{q}) - \partial_q\tilde{\mathcal{L}}(q, \dot{q}) = 0, \\ \Leftrightarrow\ &\tilde{M}(q)\ddot{q} + \tilde{C}(q, \dot{q})\dot{q} + \tilde{N}(q) = 0, \end{aligned} \tag{8}$$

where $\tilde{C}(q, \dot{q})$ and $\tilde{N}(q) = \nabla_q\tilde{\mathcal{V}}(q)$ are the closed-loop Coriolis/centrifugal matrix and gravitational forces vector, respectively.

The systems (6) and (8) match if (8) is a possible closed-loop system of (6), i.e., there exists a control law u such that (6) becomes (8). Standard results in [29] shows that these two systems match if and only if there exists a full-rank left annihilator $B(q)^\perp \in \mathbb{R}^{(n-p)\times n}$ of $B(q)$, i.e., $B(q)^\perp B(q) = 0$ and $\mathrm{rank}(B(q)^\perp) = (n-p)$, $\forall q \in \mathcal{Q}$, such that

$$B^\perp[C\dot{q} + N - M\tilde{M}^{-1}(\tilde{C}\dot{q} + \tilde{N})] = 0, \tag{9}$$

where q and $\dot{q}$ are omitted in (9) and hereafter to abbreviate notations.

Equation (9) is the so-called *matching condition*, which is a nonlinear partial differential equation that determines the achievable closed-loop energy. While (9) can be trivially satisfied for fully actuated systems, its solution can be quite difficult to obtain for underactuated system. Assuming (9) is satisfied and following the same procedure in [18], we can obtain that

$$Bu = M\ddot{q} + C\dot{q} + N - (\tilde{M}\ddot{q} + \tilde{C}\dot{q} + \tilde{N}). \tag{10}$$

Solving (8) for $\ddot{q}$, one can obtain the expression as

$$\ddot{q} = -\tilde{M}^{-1}(\tilde{C}\dot{q} + \tilde{N}). \tag{11}$$

Substituting (11) into (10) and multiplying the left-pseudo inverse of $B(q)$ (matrix inverse if $n = p$) on both sides of (10), one obtains the control law as [18]

$$u = (B^TB)^{-1}B^T[C\dot{q} + N - M\tilde{M}^{-1}(\tilde{C}\dot{q} + \tilde{N})]. \tag{12}$$

B. EQUIVALENT CONSTRAINED DYNAMICS

In this section, we review the procedure in [25] to derive the equivalent constrained dynamics (ECD). Plugging expressions for A and λ into (1), we can obtain the ECD in the form of (6) that has fewer or zero unactuated DOFs compared to the generalized dynamics (1) without constraints. The equivalent

constrained form of (1) is expressed as

$$M_\lambda \ddot{q} + C_\lambda \dot{q} + N_\lambda = B_\lambda v + J_\lambda^T F + B_\lambda u, \tag{13}$$

where

$$\begin{aligned} M_\lambda &= M, \\ C_\lambda &= (I - A^T W A M^{-1}) C + \cancel{A^T W \dot{A}}, \\ N_\lambda &= (I - A^T W A M^{-1}) N, \\ B_\lambda &= (I - A^T W A M^{-1}) B, \\ J_\lambda^T &= (I - A^T W A M^{-1}) J^T, \end{aligned} \tag{14}$$

$$W = (A M^{-1} A^T)^{-1}. \tag{15}$$

Given the open-loop dynamics (13), we define the desired closed-loop ECD as

$$\tilde{M}_\lambda \ddot{q} + \tilde{C}_\lambda \dot{q} + \tilde{N}_\lambda = \tilde{B}_\lambda v + \tilde{J}_\lambda F, \tag{16}$$

where $\tilde{M}_\lambda = \tilde{M}$ is the mass matrix in the closed-loop ECD and is assumed to be positive-definite. Ensuring this matrix to be positive-definite will be discussed later in the simulation section. The remaining terms in (16) are given by

$$\begin{aligned} \tilde{C}_\lambda &= (I - A^T \tilde{W} A \tilde{M}^{-1}) \tilde{C} + \cancel{A^T \tilde{W} \dot{A}}, \\ \tilde{N}_\lambda &= (I - A^T \tilde{W} A \tilde{M}^{-1}) \tilde{N}, \\ \tilde{B}_\lambda &= (I - A^T \tilde{W} A \tilde{M}^{-1}) \tilde{B}, \\ \tilde{J}_\lambda^T &= (I - A^T \tilde{W} A \tilde{M}^{-1}) \tilde{J}^T, \\ \tilde{W} &= (A \tilde{M}^{-1} A^T)^{-1}, \end{aligned} \tag{17}$$

where $\tilde{C}$ and $\tilde{N}$ are the dynamics terms of (1) in closed loop. We denote the closed-loop human input vector as $\tau_{\text{hum}} = \tilde{B}_\lambda v + \tilde{J}_\lambda^T F$ but make *no* assumptions on the human inputs v and F.

C. MATCHING BASED ON CONSTRAINED DYNAMICS

We begin this part by introducing the generalized matching condition based on ECD. Given (13) and (16), we follow the procedure from (6) to (9) to derive the matching condition for the ECD as

$$\begin{aligned} B_\lambda^\perp [&C_\lambda \dot{q} + N_\lambda - B_\lambda v - J_\lambda^T F \\ &+ M_\lambda \tilde{M}_\lambda^{-1} (\tilde{B}_\lambda v + \tilde{J}_\lambda^T F - \tilde{C}_\lambda \dot{q} - \tilde{N}_\lambda)] = 0, \end{aligned} \tag{18}$$

which can be separated into sub-matching conditions that correspond to matching for mechanical energy and human inputs, respectively:

$$B_\lambda^\perp [C_\lambda \dot{q} + N_\lambda - M_\lambda \tilde{M}_\lambda^{-1} (\tilde{C}_\lambda \dot{q} + \tilde{N}_\lambda)] = 0, \tag{19}$$

$$B_\lambda^\perp [B_\lambda v + J_\lambda^T F - M_\lambda \tilde{M}_\lambda^{-1} (\tilde{B}_\lambda v + \tilde{J}_\lambda^T F)] = 0. \tag{20}$$

1) Matching for Mechanical Energy

Prior research showed that the bottom-right submatrix of a mass matrix is the mass matrix of a lower-dimensional mechanical system [19]. This motivates us to shape the bottom-right part in M_λ, which may render matching conditions that are easier to satisfy. Following the procedure in [24], we decompose M_λ into matrix blocks, i.e.,

$$M = \begin{bmatrix} M_1 & M_2 \\ M_2^T & M_4 \end{bmatrix} = M_\lambda, \tag{21}$$

where $M_1 \in \mathbb{R}^{c \times c}$, $M_2 \in \mathbb{R}^{c \times (n-c)}$. We want the bottom-right part to be shaped via control, hence we define the closed-loop inertia matrix as

$$\tilde{M} = \begin{bmatrix} M_1 & M_2 \\ M_2^T & \tilde{M}_4 \end{bmatrix} = \tilde{M}_\lambda, \tag{22}$$

where the choice of $\tilde{M}_4$ will be specified later.

Note from [18] that we have the relationship between C and M as

$$C\dot{q} = D_q(M\dot{q})\dot{q} - \frac{1}{2}\partial_q(\dot{q}^T M \dot{q}), \tag{23}$$

where $D_{\mathrm{x}}(\mathrm{y})$ is the Jacobian matrix of partial derivatives of vector y with respect to vector x. Because the first c DOFs are constrained, their time-derivatives equal zero so that (23) reduces to

$$C\dot{q} = D_q \begin{bmatrix} M_2 \dot{q}_{c+1,n} \\ M_4 \dot{q}_{c+1,n} \end{bmatrix} \begin{bmatrix} 0 \\ \dot{q}_{c+1,n} \end{bmatrix} - \frac{1}{2}\partial_q(\dot{q}_{c+1,n}^T M_4 \dot{q}_{c+1,n}),$$

where the subscript (i, j) indicates rows i through j of a matrix. Note that the submatrix M_4 does not depend on $q_{1,c}$ based on the recursively cyclic property in [19], yielding simplified expressions for $C\dot{q}$ and $\tilde{C}\dot{q}$ as

$$C\dot{q} = \begin{bmatrix} \partial_{q_{c+1,n}}(M_2 \dot{q}_{c+1,n})\dot{q}_{c+1,n} \\ \Psi \end{bmatrix}, \tag{24}$$

$$\tilde{C}\dot{q} = \begin{bmatrix} \partial_{q_{c+1,n}}(M_2 \dot{q}_{c+1,n})\dot{q}_{c+1,n} \\ \tilde{\Psi} \end{bmatrix}, \tag{25}$$

where

$$\begin{aligned} \Psi &:= \frac{1}{2}\partial_{q_{c+1,n}}(\dot{q}_{c+1,n}^T M_4 \dot{q}_{c+1,n}) \in \mathbb{R}^{(n-c)\times 1}, \\ \tilde{\Psi} &:= \frac{1}{2}\partial_{q_{c+1,n}}(\dot{q}_{c+1,n}^T \tilde{M}_4 \dot{q}_{c+1,n}) \in \mathbb{R}^{(n-c)\times 1}. \end{aligned}$$

Following the same procedure in [24], we calculate $(I - A^T W A M^{-1})$ in (13) using the blockwise inversion of M and define $(I - A^T \tilde{W} A \tilde{M}^{-1})$ accordingly as

$$(I - A^T W A M^{-1}) = \begin{bmatrix} 0_{c\times c} & Y \\ 0_{(n-c)\times c} & I_{(n-c)} \end{bmatrix}, \tag{26}$$

$$(I - A^T \tilde{W} A \tilde{M}^{-1}) = \begin{bmatrix} 0_{c\times c} & \tilde{Y} \\ 0_{(n-c)\times c} & I_{(n-c)} \end{bmatrix}, \tag{27}$$

where $Y = M_2 M_4^{-1}$ and $\tilde{Y} = M_2 \tilde{M}_4^{-1}$. Multiplying (26) with (24) and (27) with (25), we obtain

$$C_\lambda \dot{q} = \begin{bmatrix} Y\Psi \\ \Psi \end{bmatrix}, \quad \tilde{C}_\lambda \dot{q} = \begin{bmatrix} \tilde{Y}\tilde{\Psi} \\ \tilde{\Psi} \end{bmatrix}. \tag{28}$$

Similarly, the constrained potential forces vectors are obtained from (15) and (17) as

$$N_\lambda = \begin{bmatrix} Y N_{c+1,n} \\ N_{c+1,n} \end{bmatrix}, \quad \tilde{N}_\lambda = \begin{bmatrix} \tilde{Y}\tilde{N}_{c+1,n} \\ \tilde{N}_{c+1,n} \end{bmatrix}. \tag{29}$$

To simplify the multiplication between M_λ and $\tilde{M}_\lambda^{-1}$, we apply the blockwise inversion method again to obtain

$$M_\lambda \tilde{M}_\lambda^{-1} = \begin{bmatrix} I_c & 0_{c\times(n-c)} \\ \Omega_1 & \Omega_2 \end{bmatrix}, \tag{30}$$

where $\Omega_1 = (I - M_4\tilde{M}_4^{-1})M_2^T(M_1 - M_2\tilde{M}_4^{-1}M_2^T)^{-1} \in \mathbb{R}^{(n-c)\times c}$ and $\Omega_2 = -\Omega_1\tilde{Y} + M_4\tilde{M}_4^{-1} \in \mathbb{R}^{(n-c)\times(n-c)}$. The matrix B_λ is calculated from (15) and its annihilator $B_\lambda^\perp$ can be chosen as

$$B_\lambda = \begin{bmatrix} YB_{c+1,n} \\ B_{c+1,n} \end{bmatrix}, \quad B_\lambda^\perp = \begin{bmatrix} I_c & -Y \\ 0_{(n-p-c)\times c} & S \end{bmatrix}, \tag{31}$$

where $S = [I_{(n-p-c)\times(n-p-c)},\ 0_{(n-p-c)\times p}]$. When the system is fully-constrained, i.e., $n = p + c$, the second block row of the annihilator disappears. It can be verified that $B_\lambda^\perp \in \mathbb{R}^{(n-p)\times n}$, $\mathrm{rank}(B_\lambda^\perp) = (n-p)$, and $B_\lambda^\perp B_\lambda = 0_{(n-p)\times p}$. Plugging $B_\lambda^\perp$, (28), (29), and (30) into (19), the left-hand side of the matching condition (19) becomes

$$\begin{aligned} &B_\lambda^\perp[C_\lambda\dot{q} + N_\lambda - M_\lambda\tilde{M}_\lambda^{-1}(\tilde{C}_\lambda\dot{q} + \tilde{N}_\lambda)] \\ &= \begin{bmatrix} I_c & -Y \\ 0_{(n-p-c)\times c} & S \end{bmatrix} \begin{bmatrix} Y(\Psi + N_\lambda) - \tilde{Y}(\tilde{\Psi} + \tilde{N}_\lambda) \\ (\Psi + N_\lambda) - (\Omega_1\tilde{Y} + \Omega_2)(\tilde{\Psi} + \tilde{N}_\lambda) \end{bmatrix} \\ &= \begin{bmatrix} I_c & -Y \\ 0_{(n-p-c)\times c} & S \end{bmatrix} \begin{bmatrix} Y\mathcal{Z} - \tilde{Y}\tilde{\mathcal{Z}} \\ \mathcal{Z} - (\Omega_1\tilde{Y} + \Omega_2)\tilde{\mathcal{Z}} \end{bmatrix}, \end{aligned} \tag{32}$$

where $\mathcal{Z} := \Psi + N_\lambda$ and $\tilde{\mathcal{Z}} := \tilde{\Psi} + \tilde{N}_\lambda$. The first c rows of (32) can be simplified as

$$\begin{aligned} &\begin{bmatrix} I_c & -Y \end{bmatrix} \begin{bmatrix} Y\mathcal{Z} - \tilde{Y}\tilde{\mathcal{Z}} \\ \mathcal{Z} - (\Omega_1\tilde{Y} + \Omega_2)\tilde{\mathcal{Z}} \end{bmatrix} \\ &= [-\tilde{Y} + Y(\Omega_1\tilde{Y} + \Omega_2)]\tilde{\mathcal{Z}} = (-\tilde{Y} + YM_4\tilde{M}_4^{-1})\tilde{\mathcal{Z}} \\ &= (-\tilde{Y} + M_2\tilde{M}_4^{-1})\tilde{\mathcal{Z}} = 0_{c\times 1}. \end{aligned} \tag{33}$$

For contacts (e.g., heel or toe contact) that result in underactuation ($n > p + c$), additional analysis is needed to fully satisfy the matching condition (19), i.e., the bottom $(n-p-c)$ rows of (32) must also be satisfied.

Note that during underactuated cases, $M_4 \in \mathbb{R}^{(n-c)\times(n-c)}$ cannot be shaped arbitrarily. We propose satisfying the matching condition by shaping only the bottom-right $p\times p$ part of M_4, which is associated with the p actuated coordinates. To show this, we first decompose and shape M_4 in a similar manner to (22) as

$$M_4 = \begin{bmatrix} M_{41} & M_{42} \\ M_{42}^T & M_{44} \end{bmatrix}, \quad \tilde{M}_4 = \begin{bmatrix} M_{41} & M_{42} \\ M_{42}^T & \tilde{M}_{44} \end{bmatrix},$$

where $M_{41} \in \mathbb{R}^{(n-p-c)\times(n-p-c)}$, $M_{42} \in \mathbb{R}^{(n-p-c)\times p}$, and $M_{44}, \tilde{M}_{44} \in \mathbb{R}^{p\times p}$. Similar to (30), the top-left element of $M_4\tilde{M}_4^{-1}$ will be $I_{(n-p-c)}$. Subtracting $M_4\tilde{M}_4^{-1}$ from $I_{(n-c)}$, the first $(n-p-c)$ rows of Ω_1 will become zeroes. As a consequence, the first $(n-p-c)$ rows of Ω_2 become $[I_{(n-p-c)},\ 0_{(n-p-c)\times p}]$. Leveraging these properties of Ω_1 and Ω_2, the bottom $(n-p-c)$ rows of (32) become

$$\begin{aligned} &\begin{bmatrix} 0_{(n-p-c)\times c} & S \end{bmatrix} \begin{bmatrix} Y\mathcal{Z} - \tilde{Y}\tilde{\mathcal{Z}} \\ \mathcal{Z} - (\Omega_1\tilde{Y} + \Omega_2)\tilde{\mathcal{Z}} \end{bmatrix} \\ &= \Psi_{1,n-p-c} - \tilde{\Psi}_{1,n-p-c} + N_{c+1,n-p} - \tilde{N}_{c+1,n-p}. \end{aligned} \tag{34}$$

From [19], we know $\partial M_{44}/\partial q_{c+1,n-p} = 0_{(n-p-c)\times 1}$, i.e., $q_{c+1,n-p}$ is cyclic in $M_{44} \in \mathbb{R}^{p\times p}$, hence $\Psi_{1,n-p-c} - \tilde{\Psi}_{1,n-p-c}$ equals $0_{(n-p-c)\times 1}$. To satisfy (34), we make the assumption $N_{c+1,n-p} = \tilde{N}_{c+1,n-p}$ as in [24], which indicates that the rows corresponding to the unactuated DOFs that are unconstrained remain unshaped. By making this assumption, (34) equals to zero and the matching condition (19) is satisfied.

2) Matching for Human Inputs

In this section we show that by shaping the bottom-right submatrix $M_{44} \in \mathbb{R}^{p\times p}$, the matching condition for human input (20) will be automatically satisfied. To begin, we separate (20) into two sub-conditions, i.e.,

$$B_\lambda^\perp(B_\lambda v - M_\lambda\tilde{M}_\lambda^{-1}\tilde{B}_\lambda v) = 0, \tag{35}$$
$$B_\lambda^\perp(J_\lambda^T F - M_\lambda\tilde{M}_\lambda^{-1}\tilde{J}_\lambda^T F) = 0. \tag{36}$$

To verify (35) holds true, plugging (30) and (31) into (35) yields

$$\begin{aligned} &B_\lambda^\perp(B_\lambda v - M_\lambda\tilde{M}_\lambda^{-1}\tilde{B}_\lambda v) = \cancel{B_\lambda^\perp B_\lambda v} - B_\lambda^\perp M_\lambda\tilde{M}_\lambda^{-1}\tilde{B}_\lambda v \\ &= \begin{bmatrix} -I_c & Y \\ 0_{(n-p-c)\times c} & -S \end{bmatrix} \begin{bmatrix} I_c & 0_{c\times(n-c)} \\ \Omega_1 & \Omega_2 \end{bmatrix} \tilde{B}_\lambda v \\ &= \begin{bmatrix} -I + Y\Omega_1 & Y\Omega_2 \\ -S\Omega_1 & -S\Omega_2 \end{bmatrix} \begin{bmatrix} 0_{c\times c} & \tilde{Y} \\ 0_{(n-c)\times c} & I_{(n-c)} \end{bmatrix} \begin{bmatrix} 0 \\ \tilde{B}_2 \end{bmatrix} v \\ &= \begin{bmatrix} -\tilde{Y} + Y\Omega_1\tilde{Y} + Y\Omega_2 \\ -S\Omega_1\tilde{Y} - S\Omega_2 \end{bmatrix} \tilde{B}_2 v. \end{aligned} \tag{37}$$

From (33), we have $-\tilde{Y} + Y\Omega_1\tilde{Y} + Y\Omega_2 = 0$, therefore the first c rows of (37) become zero. Similar to $M_\lambda\tilde{M}_\lambda^{-1}$ in (30), the first $(n-p-c)$ rows of are $[I_{(n-p-c)},\ 0_{(n-p-c)\times p}]$. Utilizing these two properties, the remaining rows of (37) become

$$\begin{aligned} &(-S\Omega_1\tilde{Y} - S\Omega_2)\tilde{B}_2 v = -SM_4\tilde{M}_4^{-1}\tilde{B}_2 v \\ &= [-I_{(n-p-c)},\ 0_{(n-p-c)\times p}] \begin{bmatrix} 0_{(n-p-c)\times p} \\ I_p \end{bmatrix} v \\ &= 0_{(n-p-c)}, \end{aligned}$$

which shows the last $(n-p-c)$ rows of (37) are zeros, i.e., (35) holds true.

To verify (36), we first calculate $B_\lambda^\perp J_\lambda^T F$ as

$$\begin{aligned} &B_\lambda^\perp J_\lambda^T F \\ &= \begin{bmatrix} I_c & -Y \\ 0_{(n-p-c)\times c} & S \end{bmatrix} \begin{bmatrix} 0_{c\times c} & Y \\ 0_{(n-c)\times c} & I_{(n-c)} \end{bmatrix} \begin{bmatrix} J_1^T \\ J_2^T \end{bmatrix} F \\ &= \begin{bmatrix} 0_{c\times c} & 0_{c\times(n-c)} \\ 0_{(n-p-c)\times c} & S \end{bmatrix} \begin{bmatrix} J_1^T \\ J_2^T \end{bmatrix} F \\ &= \begin{bmatrix} 0_{c\times 3} \\ SJ_2^T F \end{bmatrix} \end{aligned} \tag{38}$$

with $J = [J_1,\ J_2] \in \mathbb{R}^{3\times n}$, and $J_1^T \in \mathbb{R}^{c\times 3}$, $J_2^T \in$

$\mathbb{R}^{(n-c)\times 3}$. Calculating $B_\lambda^\perp M_\lambda \tilde{M}_\lambda^{-1} \tilde{J}_\lambda^T F$, we have

$$\begin{aligned} & B_\lambda^\perp M_\lambda \tilde{M}_\lambda^{-1} \tilde{J}_\lambda^T F \\ &= \begin{bmatrix} (-\tilde{Y} + Y\Omega_1 \tilde{Y} + Y\Omega_2) J_2^T \\ (-S\Omega_1 \tilde{Y} - S\Omega_2) J_2^T \end{bmatrix} F \\ &= \begin{bmatrix} 0_{c\times 3} \\ S J_2^T F \end{bmatrix}. \end{aligned} \tag{39}$$

Subtracting (39) from (38) we obtain zero, i.e., (36) holds true. Given both (35) and (36) are satisfied, we prove that the matching conditions for human input are satisfied as a consequence of shaping $M_{44} \in \mathbb{R}^{p\times p}$ despite of the forms of F and v.

Because human joint input v and the interaction forces F are not easily measured in practice, we assume human is studying the interaction with the exoskeleton and adapting their gaits accordingly. In particular, we assume that human input is mapped into the closed-loop dynamics via a specific mapping that will make v and F disappear in the control law. The control law that brings (13) into (16) then becomes

$$u = B_\lambda^+ [C_\lambda \dot{q} + N_\lambda - M_\lambda \tilde{M}_\lambda^{-1} (\tilde{C}_\lambda \dot{q} + \tilde{N}_\lambda)], \tag{40}$$

where $B_\lambda^+ = (B_\lambda^T B_\lambda)^{-1} B_\lambda^T$ is the left pseudo inverse of B_λ. Because this control law is not defined based on pre-defined trajectories or tasks, it is capable of assisting different subjects with them exhibiting their own preferred gait patterns across locomotor tasks. In Section V-D, we will see that this control law is able to provide beneficial outcome despite of the fact that human input terms are not explicitly included. Similar to [24], we can show that if (19) and (20) are satisfied, matching (13) with (17) is equivalent to bringing (1) into its desired form

$$\tilde{M}\ddot{q} + \tilde{C}\dot{q} + \tilde{N} + A^T \tilde{\lambda} = \tilde{B} v + \tilde{J}^T F \tag{41}$$

with $\tilde{\lambda}$ given as

$$\tilde{\lambda} = (A\tilde{M}^{-1}A^T)^{-1} A\tilde{M}^{-1}(\tilde{B}v + \tilde{J}^T F - \tilde{C}\dot{q} - \tilde{N}). \tag{42}$$

IV. PASSIVITY AND STABILITY

In [24], we showed that the proposed potential energy shaping law preserves a passive mapping from human inputs to joint velocity in the closed loop, based on which we highlighted Lyapunov stability with commonly assumed human policies. We now generalize these results to the case of total energy shaping during fully-actuated phases.

A. PASSIVITY OF THE HUMAN-EXOSKELETON SYSTEM

Consider the dynamics (1) of the human wearing the exoskeleton with τ on the right-hand side as an input, and let $y = h(x) \in \mathbb{R}^n$ be the output, where x denotes the system's state vector and is given as $x = (q^T, \dot{q}^T)^T \in \mathbb{R}^{2n\times 1}$. Based on [30], a kinematic chain with dynamics of the form (1) is passive from joint torque input to joint velocity output with total energy E as the storage function, i.e.,

$$\begin{aligned} \dot{E} &= \dot{q}^T M \ddot{q} + \frac{1}{2}\dot{q}^T \dot{M} \dot{q} + \dot{q}^T N \\ &= \dot{q}^T (\tau - C\dot{q} - N - A^T\lambda) + \frac{1}{2}\dot{q}^T \dot{M}\dot{q} + \dot{q}^T N \\ &= \dot{q}^T \tau + \frac{1}{2}\dot{q}^T (\dot{M} - 2C)\dot{q} + \cancel{\dot{q}^T A^T \lambda}, \end{aligned} \tag{43}$$

where the skew-symmetry property $(\dot{M} - 2C)^T = -(\dot{M} - 2C)$ has been applied, and we leveraged the fact that constraint forces do no mechanical work [28], i.e., $\dot{q}^T A^T \lambda = 0$.

For a human leg without an exoskeleton ($u = 0$), muscular input v and interaction forces F provide the torque input in the passive mapping to leg joint velocity (note that studies of passivity in human joint control date back to [31]). If an energy-shaping controller preserves this human passivity property in closed loop (Fig. 3), then energy growth of the coupled human-machine system is controlled by the human.

Lemma 1: The closed-loop energy function $\tilde{E}(q, \dot{q}) = \frac{1}{2}\dot{q}^T \tilde{M}(q)\dot{q} + \tilde{\mathcal{V}}(q)$ is positive-definite during fully-actuated phases given that $\tilde{M}$ is positive-definite.

Proof: The quadratic term $\frac{1}{2}\dot{q}^T \tilde{M}\dot{q}$ is non-negative given that $\tilde{M}$ is positive-definite, where the choice for this matrix will be specified in the simulation section. Therefore, the positive definiteness of $\tilde{E}$ relies on the positive definiteness of the shaped potential energy $\tilde{\mathcal{V}}$. The potential energy $\mathcal{V}$ can be defined in terms of the shapeable and unshapeable rows of N using the *variable gradient method* [32]:

$$\begin{aligned} \mathcal{V}(q) &= \int_0^q \sum_{j=1}^{n} N_j(s)\, \mathrm{d}s \\ &= \int_0^q \sum_{j=1}^{n-p} N_j(s)\, \mathrm{d}s + \int_0^q \sum_{j=n-p+1}^{n} N_j(s)\, \mathrm{d}s \\ &:= \mathcal{V}_1(q) + \mathcal{V}_2(q), \end{aligned} \tag{44}$$

where s is the integration variable. Similar to [25], we define $\tilde{N}$ in a way such that BWS can be provided, i.e., the following properties hold for $\tilde{N}$:

$$\tilde{N}_{1,n-p} = N_{1,n-p}, \quad \tilde{N}_{n-p+1,n} = \mu N_{n-p+1,n}, \tag{45}$$

where $\mu := \frac{\tilde{g}}{g}$ is a strictly positive number defined as the ratio between the shaped and the original gravity parameters. Given (44) and (45), we can obtain the shaped potential energy

$$\begin{aligned} \tilde{\mathcal{V}}(q) &= \int_0^q \sum_{j=1}^{n-p} N_j(s)\mathrm{d}s + \int_0^q \sum_{j=n-p+1}^{n} \tilde{N}_j(s)\mathrm{d}s \\ &= \int_0^q \sum_{j=1}^{n-p} N_j(s)\mathrm{d}s + \mu \int_0^q \sum_{j=n-p+1}^{n} N_j(s)\mathrm{d}s \\ &= \mathcal{V}_1(q) + \mu \mathcal{V}_2(q). \end{aligned} \tag{46}$$

Note that $\tilde{\mathcal{V}}(q)$ defined in (46) is valid only during fully-actuated phases, i.e., the desired gravitational forces vector $\tilde{N}$ satisfies the symmetric requirement $\frac{\partial \tilde{N}}{\partial q}^T = \frac{\partial \tilde{N}}{\partial q}$ in [32]. For defining valid potential energy during underactuated phases,

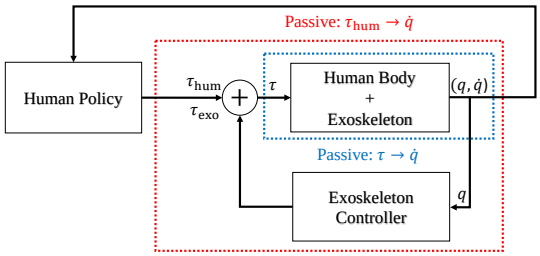

FIGURE 3. Feedback loops and passive mappings of a human wearing an energy-shaping exoskeleton. This figure is reproduced from [24].

the readers are referred to the definition in [33]. Given (46), the shaped total energy takes the following form:

$$\tilde{E}(q,\dot{q}) = \frac{1}{2}\dot{q}^T\tilde{M}(q)\dot{q} + \mathcal{V}_1(q) + \mu\mathcal{V}_2(q).$$

We set the datum for potential energy such that the potential energy $\mathcal{V}$ equals zero only at the datum, and for other configurations we have $\mathcal{V}_1 > 0$ and/or $\mathcal{V}_2 > 0$. It is then easy to see that $\mathcal{V}_1 + \mu\mathcal{V}_2 = 0$ at the datum and $\mathcal{V}_1 + \mu\mathcal{V}_2 > 0$ at all other configurations with $\mu > 0$. Given that the kinetic energy $\frac{1}{2}\dot{q}^T\tilde{M}(q)\dot{q}$ is non-negative, the overall shaped energy is positive definite. ■

Note that in order to retrieve a valid closed-loop potential energy, the definition of $\tilde{N}$ needs to satisfy the symmetric Jacobian matrix requirement in [32]. The definition of $\tilde{N}$ in this paper only satisfies this requirement during fully-actuated phases. However, we can still prove that $\tilde{E}$ is positive-definite during underactuated phases following the definition of $\tilde{N}$ presented in [33].

Theorem 1: Given positive-definite $\tilde{M}$, the closed-loop system (41) is passive from closed-loop human input $\tau_{\text{hum}} = \tilde{B}v + \tilde{J}^T F$ to the joint velocity output $y = \dot{q}$ with storage function $\tilde{E}$, i.e., $\frac{\mathrm{d}}{\mathrm{d}t}\tilde{E} = \dot{q}^T\tau_{\text{hum}}$.

Proof: The non-negativity requirement of a storage function is satisfied by Lemma 1. The same procedure as (43) with closed-loop dynamics (41) yields $\frac{\mathrm{d}}{\mathrm{d}t}\tilde{E} = \dot{q}^T\tau_{\text{hum}}$. ■

This passive relationship indicates that human will control the energy growth of the human-exoskeleton system, therefore ensuring the safety of human-robot interaction.

B. STABILITY OF THE HUMAN-EXOSKELETON SYSTEM

In this section, we highlight two stability results during fully-actuated phases assuming the human is modulating the stiffness and viscosity of a joint [31], [34]. Similar to [24], we first consider feedback control with only the passive output (i.e., joint velocity) and then we consider the more general case with joint stiffness. We first state a standard result from [35] as:

Proposition 1: Consider the passive system (41) with input τ_{hum} and output $y = \dot{q}$. Given output feedback control $\tau_{\text{hum}} = \sigma(y)$, where σ is any continuous function satisfying $y^T\sigma(y) \leq 0$, then $\lim_{t\to\infty} y(t) \to 0$ and the origin $(q,\dot{q}) = (0,0)$ is *stable in the sense of Lyapunov*.

Therefore, if we assume the human input takes the form $\tau_{\text{hum}} = -K_{\text{d}}\dot{q}$, where $K_{\text{d}} \in \mathbb{R}^{n\times n}$ is a positive semi-definite diagonal matrix. From Theorem 1 we will have

$$\dot{\tilde{E}} = -\dot{q}^T K_{\text{d}}\dot{q} \leq 0,$$

and thus convergence of the joints and Lyapunov stability of the upright posture (the origin).

Now consider a human impedance controller with viscosity given as:

$$\tau_{\text{hum}} = -K_{\text{p}}e - K_{\text{d}}\dot{e}, \tag{47}$$

where $K_{\text{p}} \in \mathbb{R}^{n\times n}$ is a positive semi-definite diagonal matrix, $e := q - \bar{q}$ represents the different between q and the fixed constant vector $\bar{q}$. We will eventually use (47) as the human input for simulating different strategies.

We can also prove the stability of the closed-loop human-exoskeleton system around the equilibrium point $(q^*, 0)$, where $(q^*, 0)$ is the state that $\tilde{N}(q^*) + A^T\tilde{\lambda} + K_{\text{p}}(q^* - \bar{q}) = 0$, i.e., the forces along the shaped potential energy balance the muscular spring forces and the ground reaction forces. To begin, we define the Lyapunov function to be $V(q,\dot{q}) = \tilde{E} + \int_{q_0}^{q} A^T\tilde{\lambda}(s,0)\mathrm{d}s + \frac{1}{2}e^T K_{\text{p}}e - \bar{V}$, where q_0 is the initial posture and $\bar{V}$ is a constant such that $\bar{V} = \tilde{E}(q^*,0) + \frac{1}{2}(q^* - \bar{q})^T K_{\text{p}}(q^* - \bar{q})$.

Lemma 2: The Lyapunov function $V(q,\dot{q})$ is locally positive definite around the equilibrium point $(q^\star, 0)$ in the tangent bundle $T\mathcal{Q}$.

Proof: The Lyapunov function $V(q,\dot{q})$ attains its minimum at $\partial V_q(q,\dot{q}) = 0$ and $\partial V_{\dot{q}}(q,\dot{q}) = 0$, i.e., $\dot{q} = 0$ and $\tilde{N} + K_{\text{p}}e + A^T\tilde{\lambda} = 0$, which corresponds to the equilibrium point $(q^*, 0)$. At this point, we have the minimal value of $V(q,\dot{q})$ as $\tilde{E}(q^*,0) + \frac{1}{2}(q^* - \bar{q})^T K_{\text{p}}(q^* - \bar{q}) - \bar{V} = 0$, where $\int_{q_0}^{q} A^T\tilde{\lambda}(s,0)\mathrm{d}s = 0$ due to the fact that constraints forces do no work [28]. Therefore, $\forall(q,\dot{q}) \neq (q^*,0) \in T\mathcal{Q}$, we have $V(q,\dot{q}) > 0$. ■

With V being a proper Lyapunov function, we take the time derivative of $V(q,\dot{q})$ with closed-loop dynamics (41) and following derivation in (43) to obtain

$$\begin{aligned}\dot{V}(q,\dot{q}) &= \dot{q}^T\tilde{M}\ddot{q} + \frac{1}{2}\dot{q}^T\dot{\tilde{M}}\dot{q} + \dot{q}^T\tilde{N} + \dot{e}^T K_{\text{p}}e \\ &= \dot{q}^T\tau_{\text{hum}} + \dot{e}^T K_{\text{p}}e \\ &= \dot{q}^T(-K_{\text{p}}e - K_{\text{d}}\dot{e} + K_{\text{p}}e) \\ &= -\dot{q}^T K_{\text{d}}\dot{q} \leq 0,\end{aligned} \tag{48}$$

implying that the equilibrium point of the shaped human exoskeleton system is Lyapunov stable [28].

V. SIMULATION RESULTS AND DISCUSSION

For studying the effects of the proposed shaping strategies during simulated walking, we consider the coupled dynamics of the two legs shown in Fig. 1, which is termed as the full biped model and is modeled as a kinematic chain with respect to the IRF defined at the stance heel. The configuration vector of the full biped model is given as $q_{\text{e}} = (\theta_{\text{x}}, \theta_{\text{y}}, \theta_{\text{ab}}, q_s^T)^T = (p_{\text{x}}, p_{\text{y}}, \phi, \theta_{\text{a}}, \theta_{\text{k}}, \theta_{\text{h}}, \theta_{\text{sk}}, \theta_{\text{sa}})^T \in \mathbb{R}^{8\times 1}$, where the definitions

for joint angles are given in Fig. 1. In this section we simulate the full biped wearing a bilateral exoskeleton with different energy shaping strategies, where the model and simulation parameters are shown in Table 2.

A. IMPEDANCE CONTROL FOR HUMAN INPUTS

In order to predict the effects of the proposed control approach, we must first construct a human-like, stable walking gait in simulation. According to the results in [36], a simulated 7-link biped can converge to a stable, natural-looking gait using joint impedance control. Therefore, we assume that the human has input torques at the ankle, knee and hip joints, and each joint torque takes the form of a set-point impedance controller. For simplicity, we keep the gains of these impedance controllers constant instead of having a different set of parameters with respect to each phase of stance. The human input vector $\tau_{\rm hum}$ for the full biped model is given as

$$\tau_{\rm hum}^T = [0_{1\times 3}, -(q_{\rm ei} - \bar{q}_{\rm ei})^T K_{\rm pi}^T - \dot{q}_{\rm ei}^T K_{\rm di}^T]^T, \qquad (49)$$

where $i = \{\rm a, k, h, sk, sa\}$. Parameters $K_{\rm pi}$, $K_{\rm di}$, $q_{\rm ei}$, and $\bar{q}_{\rm ei}$ are constant values corresponding to the stiffness, viscosity, actual angle, and equilibrium angle of each joint, respectively. This particular form of human input is merely an assumption we made to simulate human walking, which does not represent real human joint torques. The proposed approach is not confined to any forms of human joint torques. Later on in Section V-D we will see beneficial results of the proposed approach using an able-bodied human subject's kinematic data.

B. HYBRID DYNAMICS AND ORBITAL STABILITY

Biped locomotion can be modeled as a hybrid dynamical system that includes continuous and discrete dynamics. Impacts happen when the swing heel contacts the ground and subsequently when the flat foot impacts the ground. The corresponding impact equations map the state of the biped at the instant before impact to the state at the instant after impact. Note that no impact occurs when switching between the flat foot and toe contact configurations. The hybrid dynamics and impact maps during one step are computed in the following sequence [25]:

1. $\mathcal{M}\ddot{q}_{\rm e} + \mathcal{N} + A_{\rm heel}^T\lambda = \tau_{\rm e}$ if $a_{\rm flat} \neq 0$,
2. $\dot{q}_{\rm e}^+ = (I - \mathcal{W}(A_{\rm flat}\mathcal{W})^{-1}A_{\rm flat})\dot{q}_{\rm e}^-$ if $a_{\rm flat} = 0$,
3. $\mathcal{M}\ddot{q}_{\rm e} + \mathcal{N} + A_{\rm flat}^T\lambda = \tau_{\rm e}$ if $|c_{\rm p}(q_{\rm e}, \dot{q}_{\rm e})| < l_{\rm f}$,
4. $\dot{q}_{\rm e}^+ = \dot{q}_{\rm e}^-, (q_{\rm e}(1)^+, q_{\rm e}(2)^+)^T = \mathcal{R}$ if $|c_{\rm p}(q_{\rm e}, \dot{q}_{\rm e})| = l_{\rm f}$,
5. $\mathcal{M}\ddot{q}_{\rm e} + \mathcal{N} + A_{\rm toe}^T\lambda = \tau_{\rm e}$ if $\mathcal{H}(q_{\rm e}) \neq 0$,
6. $(q_{\rm e}^+, \dot{q}_{\rm e}^+) = \mathcal{D}(q_{\rm e}^-, \dot{q}_{\rm e}^-)$ if $\mathcal{H}(q_{\rm e}) = 0$,

where this sequence of continuous and discrete dynamics repeats after a complete step, i.e., phase 6 switches back to phase 1 for the next step. The matrix $\mathcal{M} \in \mathbb{R}^{8\times 8}$ is the inertia matrix of the full biped model, and $\mathcal{N} \in \mathbb{R}^{8\times 1}$ groups the model's Coriolis and gravitational forces. The terms $A_{\rm heel}$, $A_{\rm flat}$ and $A_{\rm toe} \in \mathbb{R}^{c\times 8}$ denote the constraint matrices for the heel contact, flat foot, and toe contact conditions depicted in Fig. 2, respectively, and the superscripts "-" and "+" indicate values before and after each impact, respectively. The term $\mathcal{R} = [l_{\rm f}\cos(\gamma), l_{\rm f}\sin(\gamma)]^T$ models the change in IRF for foot length $l_{\rm f}$. Note that $\mathcal{W} = \mathcal{M}^{-1}A_{\rm flat}^T$, and the vector $c_{\rm p}(q_{\rm e}, \dot{q}_{\rm e})$ is the COP defined with respect to the heel IRF calculated using the conservation law of momentum. The ground clearance of the swing heel is denoted by $\mathcal{H}(q_{\rm e})$, and $\mathcal{D}_{\rm e}$ denotes the swing heel ground-strike impact map based on [37]. The overall torque input $\tau_{\rm e} \in \mathbb{R}^{8\times 1}$ consists of both the human input vector $\tau_{\rm hum} \in \mathbb{R}^{8\times 1}$ and the robotic input vector $\tau_{\rm exo} \in \mathbb{R}^{8\times 1}$.

Due to the difficulty of analytically proving stability for hybrid systems in general, we checked local stability numerically by applying the Poincaré method. Letting $x_{\rm e} = (q_{\rm e}^T, \dot{q}_{\rm e}^T)^T$ be the state vector of the full biped, a walking gait corresponds to a periodic solution curve $\bar{x}_{\rm e}(t)$ of the hybrid system such that $\bar{x}_{\rm e}(t) = \bar{x}_{\rm e}(t+T)$, for all $t \geq 0$ and some minimal $T > 0$. The set of states occupied by the periodic solution defines a periodic orbit $\mathcal{O} := \{x_{\rm e} | x_{\rm e} = \bar{x}_{\rm e}(t) \text{ for some } t\}$ in the state space. The step-to-step evolution of a solution curve can be modeled with the *Poincaré* map $\mathcal{P} : \mathcal{S} \to \mathcal{S}$, where $\mathcal{S} = \{x_{\rm e} | \mathcal{H}(q_{\rm e}) = 0\}$ is the switching surface indicating initial heel contact. The intersection of a periodic orbit with the switching surface is a fixed point $x_{\rm e}^* = \mathcal{P}(x_{\rm e}^*)$. We can linearize the Poincaré map about this point to analyze the local stability of the hybrid dynamical system according to the standard result in [37]. If the eigenvalues of the Jacobian $\nabla_{x_{\rm e}}\mathcal{P}(x_{\rm e}^*)$ are within the unit circle, where $x_{\rm e}^* = G \cap \mathcal{O}$, then the periodic orbit $\mathcal{O}$ is locally exponentially stable in the hybrid system. The eigenvalues are calculated in simulation by first allowing the biped to converge to a fixed point and then by performing the perturbation analysis similar to [37].

C. ENERGY SHAPING STRATEGIES

In Section III, we satisfied the matching conditions without specifying the choices of $\tilde{\mathcal{M}}_4$ and $\tilde{N}$. In this section, we will propose a specific way to define these two terms and simulate the associated shaping strategies as a case study.

Prior work in [12] indicates that inertia compensation can counteract the side effects of the exoskeleton inertia on human legs during walking. Based on this fact, we wish to define the closed-loop dynamics with reduced mass and inertia parameters so that assistance can be produced through the actuators of an exoskeleton. However, the inertia matrix $\tilde{\mathcal{M}}$ may not remain positive-definite given arbitrary reduced mass and/or inertial parameters in $\tilde{\mathcal{M}}_4$. Therefore, we need to ensure $\tilde{\mathcal{M}} > 0$, i.e., $\tilde{\mathcal{M}}$ is positive definite while reducing its parameters.

1) Ensuring Positive Definiteness of $\tilde{\mathcal{M}}$

One interesting property about the inertia matrix is that the mass and inertial terms show up following a "cyclic-like property" as discussed in [19], i.e., the number of links whose parameters show up in the matrix gradually decreases when traversing from the top-left corner to the bottom-right corner

of the mass matrix. This suggests that each "layer" of the matrix carries a different weight in the overall kinetic energy. Motivated by this fact, we defined $\tilde{\mathcal{M}}_4 \in \mathbb{R}^{5\times5}$ as:

$$\begin{bmatrix} k_1\cdot\mathcal{M}_{(4,4)} & k_1\cdot\mathcal{M}_{(4,5)} & \dots & k_1\cdot\mathcal{M}_{(4,8)} \\ k_1\cdot\mathcal{M}_{(5,4)} & k_2\cdot\mathcal{M}_{(5,5)} & \dots & k_2\cdot\mathcal{M}_{(5,8)} \\ \vdots & \vdots & \ddots & \vdots \\ k_1\cdot\mathcal{M}_{(8,4)} & k_2\cdot\mathcal{M}_{(8,5)} & \dots & k_5\cdot\mathcal{M}_{(8,8)} \end{bmatrix}, \quad (50)$$

where $0 < k_i \leq 1$ is the parameter that needs to be determined. To ensure $\tilde{\mathcal{M}}$ is positive definite, we can formulate this problem as finding possible parameter sets $K = [k_1, k_2, \dots, k_5]^T \in \mathbb{R}^{5\times1}$ such that the eigenvalues of $\tilde{\mathcal{M}}$ stay strictly positive given constraints on k_i and joint position $q_e(j)$, i.e.,

$$\text{eig}(\tilde{\mathcal{M}}(q_e)) > 0,$$
$$\text{subject to } \begin{cases} q_e(j) \in [-\frac{\pi}{2}, \frac{\pi}{2}], & j = 1,2,\dots,8 \\ 0 < k_i \leq 1, & i = 1,2,\dots,5 \end{cases}$$

To find solutions for k_i, we adopted the model and simulation parameters from [25] and used the MATLAB function **fmincon** to find the minimized eigenvalues of $\tilde{\mathcal{M}}$ with constraints on $q_e(j)$. The values of k_i that ensures these minimized eigenvalues being strictly positive are shown in Table 1. Note that we have constrained the range for each joint variable $q_e(j)$ to be within $[-\frac{\pi}{2}, \frac{\pi}{2}]$, which is sufficient to cover the range for common locomotor tasks [38]. Additionally, even if the inertial parameters differ from the true values of human anatomical parameters, with a given set of inertial parameters, the positive definiteness of $\tilde{\mathcal{M}}$ can still be ensured. In practical application where human anatomical parameters are unknown, we can apply range constraints on these parameters in addition to the constraints on angles and repeat the calculation again to find the values of k_i. We can increase ranges for these constraints to obtain more accurate results for k_i.

TABLE 1. Solutions of $0 < k_i \leq 1$ that ensure $\tilde{\mathcal{M}}$ is positive definite

k_1	k_2	k_3	k_4	k_5
1	1	1	1	[0.6, 0.9]
1	1	1	0.9	[0.5, 1]
1	1	1	0.8	[0.6, 1]
1	1	0.9	1	[0.6, 1]
1	1	0.9	0.9	[0.5, 1]
1	1	0.9	0.8	[0.5, 1]
1	1	0.9	0.7	[0.6, 1]

2) Notation for Shaping Strategies

To conduct simulations, we chose two sets of parameters

$$K_1 = [1, 1, 0.9, 0.8, 0.5]^T, \quad K_2 = [1, 1, 0.9, 1, 0.6]^T.$$

from Table 1 to define $\tilde{\mathcal{M}}_4$ with reduced mass and inertia parameters. For comparative purposes, we also chose $K_3 = [1, 1, 1.1, 1.2, 1.5]^T$ and $K_4 = [1, 1, 1.1, 1, 1.4]^T$ to add virtual mass and inertia in $\tilde{\mathcal{M}}_4$. For notational purposes, $0 \leq k_i < 1$ indicates that we are providing $(1 - k_i)\cdot100\%$ support for compensating limb mass and inertia, whereas $k_i > 1$ indicates we are adding $(k_i - 1)\cdot100\%$ virtual limb mass and inertia in closed loop. We chose $k_i \geq 1$ to virtually challenge the subject, as evidence in [39] suggests that adding functional resistance to a subject's lower limbs can account for specific strength deficits during walking. As for $\tilde{N}$, we chose $\mu = 1.15$ for negative BWS ($\tilde{g} > g$) and $\mu = 0.85$ for positive BWS ($\tilde{g} < g$). To simplify notation, we name different shaping strategies as "A/R (strategy parameters)", where "A" is the abbreviation for "Assistive" and corresponds to the case where $0 < k_i \leq 1$ and/or $\mu < 1$. The letter "R" is the abbreviation for "Resistive" and corresponds to the case where $k_i > 1$ and/or $\mu > 1$. For example, "A (K_1)" indicates assistive kinetic energy shaping with parameter K_1, and "R ($K_4, \mu = 1.15$)" indicates resistive total energy shaping with parameters K_4 and $\mu = 1.15$.

TABLE 2. Model and Simulation Parameters

Parameter	Variable	Value
Hip mass	m_h	31.73 [kg]
Thigh mass	m_t	9.457 [kg]
Shank mass	m_s	4.053 [kg]
Foot mass	m_f	1 [kg]
Thigh moment of inertia	I_t	0.1995 [kg·m^2]
Shank moment of inertia	I_s	0.0369 [kg·m^2]
Full biped shank length	l_s	0.428 [m]
Full biped thigh length	l_t	0.428 [m]
Full biped heel length	l_a	0.07 [m]
Full biped foot length	l_f	0.2 [m]
Slope angle	γ	0.095 [rad]
Hip equilibrium angle	$\bar{q}_{eh}$	−0.5 [rad]
Hip proportional gain	K_{ph}	182.250 [N·m/rad]
Hip derivative gain	K_{dh}	35.1 [N·m·s/rad]
Swing knee equilibrium angle	$\bar{q}_{esk}$	0.2 [rad]
Swing knee proportional gain	K_{psk}	182.258 [N·m/rad]
Swing knee derivative gain	K_{dsk}	18.9 [N·m·s/rad]
Swing ankle equilibrium angle	$\bar{q}_{sa}$	−0.25 [rad]
Swing ankle proportional gain	K_{psa}	182.250 [N·m/rad]
Swing ankle derivative gain	K_{dsa}	0.81 [N·m·s/rad]
Stance ankle equilibrium angle	$\bar{q}_{ea}$	0.01 [rad]
Stance ankle proportional gain	K_{pa}	546.75 [N·m/rad]
Stance ankle derivative gain	K_{da}	21.257 [N·m·s/rad]
Stance knee equilibrium angle	$\bar{q}_{ek}$	−0.05 [rad]
Stance knee proportional gain	K_{pk}	546.75 [N·m/rad]
Stance knee derivative gain	K_{dk}	21.278 [N·m·s/rad]

D. RESULTS AND DISCUSSION

We followed the same procedure presented in [25] to first tune the human joint impedance by trial and error to find a stable nominal gait. Once the stable nominal gait was found, these impedance parameters were kept constant to isolate the effects of different energy shaping controllers. Then, we plugged in (50) and (45) into (40) to obtain the control law for our simulation. During simulation, we first set $\mu = 1$ so that $\tilde{N} = N$ and progressively changed k_i to study the effects of kinetic energy shaping on the biped. Then, we fixed $k_i = 1$ and altered μ to see the independent effects of potential energy shaping. Finally, we increased or decreased both terms concurrently to observe the effects of total energy shaping.

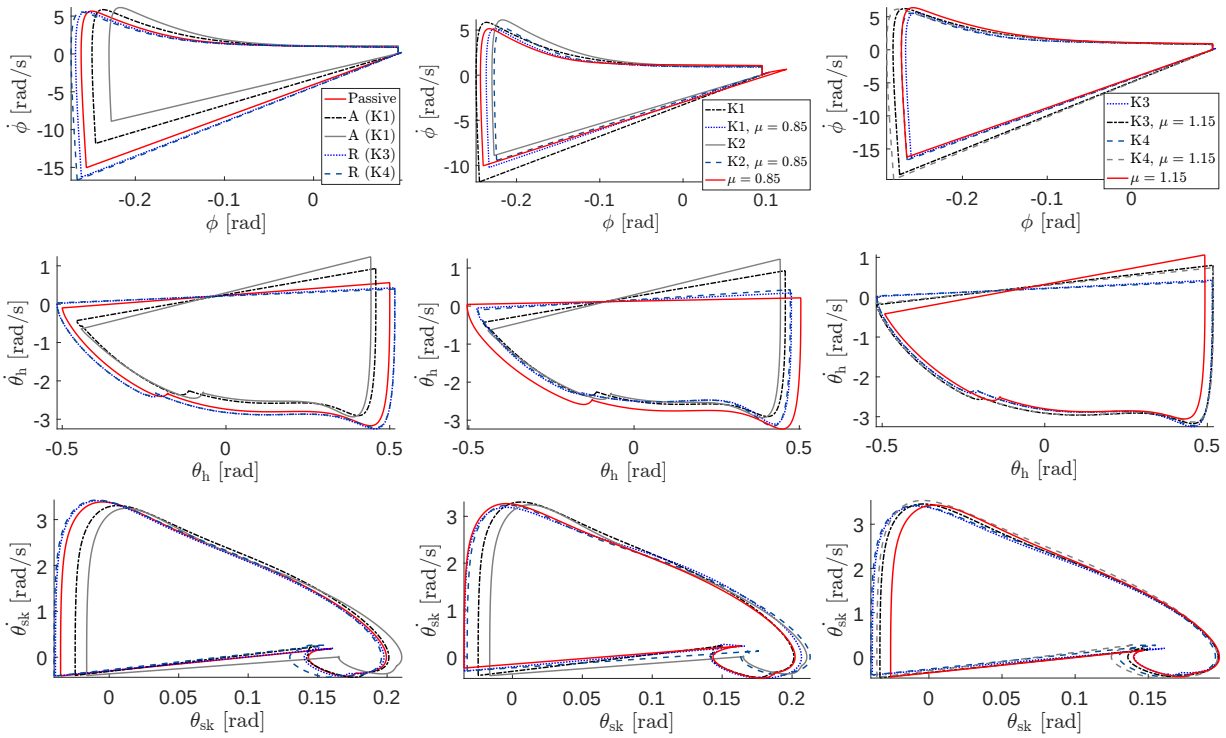

FIGURE 4. Phase portraits of ϕ, θ_{h}, and θ_{sw} with different shaping strategies indicated by "A" (Assistive) or "R" (Resistive) along with the scaling factor of shaped energies in the parentheses. The left column compares the phase portraits of the passive gait with different shaped gaits, and the center and right columns compare the phase portraits with different assistive and resistive strategies, respectively with "A" and "R" omitted in the figure legend. Each column shares the same legend shown in the top figure.

For each specific combination of K and μ, we allowed the biped to converge to a steady gait before recording data.

1) Phase Portraits

For a joint-level perspective, Fig. 4 compares the phase portraits of the passive gait and the shaped gaits with different shaping strategies. Wider orbits for all joints correspond to longer steps and taller orbits for all joints correspond to faster steps. For cases "A (K_1)" and "A (K_2)", compensating virtual mass and inertia provides less range of motion and slower joint velocities compared to the passive gait. The opposite effect is observed for the cases of "R (K_3)" and "R (K_4)" that virtually add limb mass and inertia. The center columns of Fig. 4 compare the phase portraits with kinetic energy shaping, potential energy shaping, and total energy shaping with *assistive* strategies. We can infer from these figures that shaping the total energy can further constrict joint motion and velocity compared to just shaping the potential or the kinetic energy, i.e., the phase portraits of solely shaping the kinetic or potential energy encompass the phase portraits of total energy shaping. Similarly, the right columns of Fig. 4 show that the phase portraits with total energy shaping are the largest among all of the *resistive* strategies that adds virtual mass and/or inertia. These phenomena are beneficial for gait training and augmentation because greater human body energetics can be shaped to allow more drastic dynamical changes on the joints compared to only shaping the potential energy [24] or only compensating for the lower-limb inertia as in [25].

2) Gait Characteristics

We also recorded the step length and step linear velocities during simulation once steady walking was achieved, where the results are shown in Table 3. From this table, we can see that by compensating for the mass and inertia parameters via kinetic energy shaping ("A (K_1)" and "A (K_3)"), the biped has shorter and slower steps compared to the passive gait, whereas adding the mass and inertia parameters ("R (K_3)" and "R (K_4)") yields faster and longer steps.

TABLE 3. Step length and step linear velocity recorded in simulation with different shaping strategies.

Control strategies	Step length [m]	Step linear velocity [m/s]
Passive ($\mu = K = 1$)	0.53	1.01
A (K_1)	0.48	0.98
A (K_2)	0.44	1.00
R (K_3)	0.55	1.02
R (K_4)	0.56	1.02
A ($K_1, \mu = 0.85$)	0.48	0.87
A ($K_2, \mu = 0.85$)	0.47	0.87
R ($K_3, \mu = 1.15$)	0.57	1.16
R ($K_4, \mu = 1.15$)	0.58	1.15

For total energy shaping cases "A ($K_1, \mu = 0.85$)" and "A ($K_2, \mu = 0.85$)", although the biped's step length remains close to the case of solely shaping the kinetic energy with K_1 and K_2, the step linear velocity of the biped drops drastically.

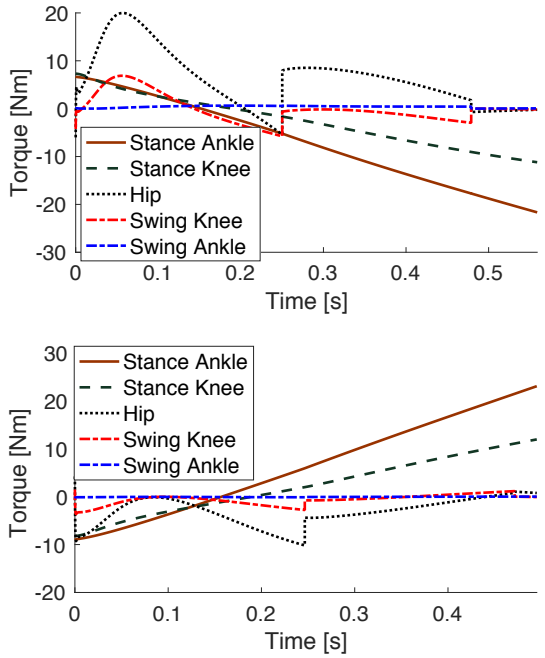

FIGURE 5. Exoskeleton torque for cases "A $(K_1, \mu = 0.85)$" (top) and "R $(K_3, \mu = 1.15)$" (bottom) during one steady step. For both figures, directions of the exoskeleton torques align with the human torques shown in Fig. 7.

Similar observations can be made for the resistive cases "R $(K_3, \mu = 1.15)$" and "R $(K_4, \mu = 1.15)$"; total energy shaping renders greater increments in step linear velocity compared to the case of solely shaping the kinetic energy. This indicates that total energy shaping can further affect the biped's step linear velocity compared to shaping the kinetic energy alone. Depending on the goal for gait training, the most appropriate shaping strategies can be chosen and adjusted to promote different gait characteristics.

3) Simulated Human and Exoskeleton Torques

To further study the effects of the proposed shaping strategies on human walking, we plotted the human hip, stance knee, and swing knee torques with different strategies during one steady step in Fig. 7. From this figure, we can see that the absolute value of the assisted human torque is tended to be smaller than the passive ones. This indicates that the proposed assistive strategies via total energy shaping can possibly augment the human muscle forces during walking. In the contrast, the magnitude of human torques with resistive strategies were greater than the passive ones, indicating that resistive strategies can force the human to expend more effort during walking.

We also plotted the exoskeleton torque with cases "A $(K_1, \mu = 0.85)$" and "R $(K_3, \mu = 1.15)$" during one steady step, where the results are shown in Fig. 5. Within one steady step, the assistive shaping strategy performs negative net work by removing the total energy, whereas the resistive strategy does the opposite by injecting total energy. The work done by the exoskeletons was -0.163 J/kg for the assistive strategy

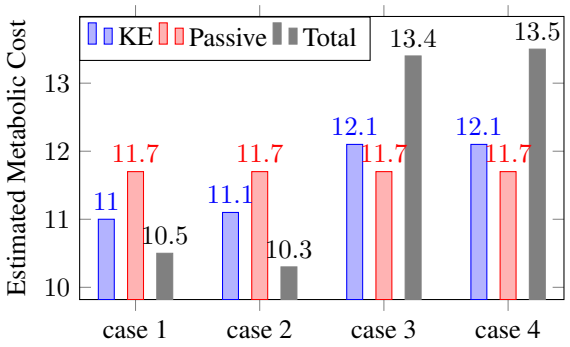

FIGURE 6. The estimated metabolic costs with different shaping strategies. The parameter K_i was used for kinetic energy shaping in case i. For potential energy shaping, $\mu = 0.85$ and $\mu = 1.15$ were used for the first and last two cases, respectively. Numbers on top of each bar denotes the sum of (51) for all actuated human joints.

and 0.140 J/kg for the resistive strategy (with 0 J/kg for the passive gait), and the overall mass for the biped is 60.75 kg. Based on [40], human muscles perform negative work per step during ramp and stair descent tests. This indicates that the assistive strategy doing negative work can assist human subjects to dissipate energy during down slope walking, which may eventually lead to metabolic reduction (see Section V-4). Similarly, authors in [41] showed that the generator of the proposed unpowered exoskeleton is able to harvest kinetic energy for generating electricity, which can be used to power the wearable electronics. This result enables the possibility of applying the proposed assistive strategy on our exoskeleton [42] to generate electricity during periods of negative work, which may help extend the exoskeleton's battery duration in practice.

4) Metabolic Cost

A key metric for evaluating an exoskeleton is whether it reduces the human user's metabolic cost of walking [14]. The integral of the squared electromyography (EMG) readings from the soleus and vastus lateralis muscles are a good representation of total metabolic cost [43]. Assuming EMG (or human muscle) activation is directly related to joint torque production, the authors of [44] proposed a simulation-based metric for metabolic cost

$$\alpha_j^2 = \frac{\int_0^T v_j^2(t)\mathrm{d}t}{T(mgl)^2} \approx \frac{\sum_{i=1}^{N_T} v_j^2(i)\Delta t(i)}{T(mgl)^2}, \qquad (51)$$

where T is the step time period, N_T is the number of timesteps in the simulation, v_j is the joint moment, $\Delta t(i)$ is the i-th timestep, m is the overall mass of the biped, and l is the length of the biped leg. We chose the nondimensionalized torque square (51) to isolate the effects of changing gait characteristics such as gait speed so that metabolic costs can be compared across different shaping strategies.

During simulation, we first allowed the biped's gait to converge to a stable limit cycle given an energy shaping strategy. By plugging energy shaping strategies (i.e., τ_{exo}) into the overall dynamics, we altered the kinematics of the

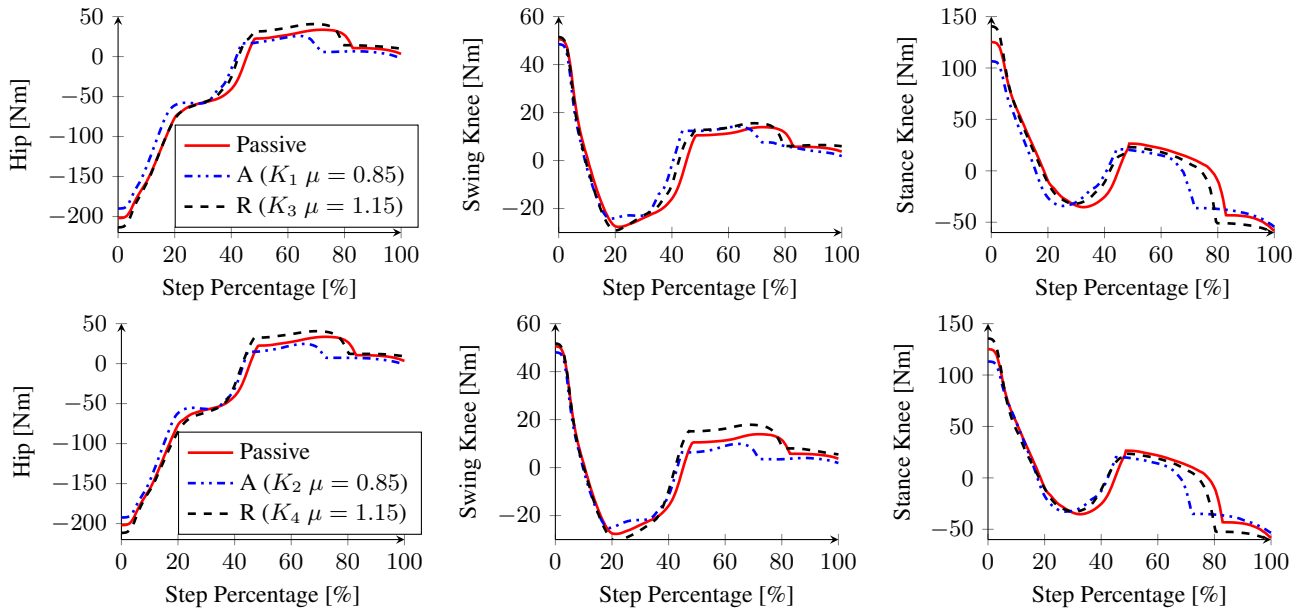

FIGURE 7. Simulated human torque $\tau_{\mathrm{h}}, \tau_{\mathrm{k}}, \tau_{\mathrm{sk}}$ of the passive, assistive, and resistive gaits during one steady step. Each data point on the curve was recorded once steady gait was achieved. For the stance/swing knee torque, positive indicates extension/flexion whereas negative indicates flexion/extension, respectively. The hip torque in the figure is the inter-leg torque instead of individual's real hip torque with positive indicating extension and negative indicating flexion.

biped in the closed loop, which were recorded once steady-state walking has been achieved. Based on these closed-loop kinematics, we computed the closed-loop human joint torques v_j given in (49) and summed them up to be all human joint costs. These costs were then plugged into (51) to estimate the effects of energy shaping on the metabolic cost of walking, where different cases are shown in Fig. 6.

From this figure, we can see that all of the assistive strategies reduce the metabolic cost compared to the passive gait, whereas all resistive strategies increase the metabolic cost. This meets our expectation that offloading the weight and inertia of a patient makes it easier to practice walking, and adding resistance to a patient makes the subject consume more energy. It is worth noting that compensating limb mass and inertia in $\tilde{\mathcal{M}}_4$ in addition to gravity by total energy shaping consumed less (more) energy compared to the cases of solely shaping the kinetic energy with assistive (resistive) strategies. These results suggest that the energy shaping approach could provide meaningful assistance during gait rehabilitation, where a clinician can adjust the scaling factors to actively manipulate human effort.

5) Normative Kinematic Data

To further verify the efficacy of the proposed approach, we examined the exoskeleton torques with able-bodied human subject's kinematic data from [45], where the results are shown in Fig. 8. The able-bodied subject in [45] was walking on a treadmill with different incline angles (-10°, 0°, 10°) at 1.2 m/s, and the kinematic data was recorded once steady walking has been achieved. From Fig. 8, we can see that all assistive ankle torques closely match the human torques. These assistive strategies provide the necessary dorsiflexion torque at terminal stance in all three tasks to help propel the subject's body forward. On the contrary, resistive ankle torques have opposite shapes compared to the human torques to add extra load for users when completing locomotor tasks. Compared to the potential energy shaping method introduced in [24], the proposed approach provides mild assistance at terminal stance instead of torques with aggressive magnitudes, which can be dangerous to human subjects. The assistive strategies for the knee joint at terminal stance has an opposite sign compared to the human torque, which is counterproductive. This will be discussed with details in Section VI. We also calculated the work done by the exoskeleton within a step by inputting the same able-bodied human subjects' passive gait data. By assuming that these subjects' joint kinematics do not change much in the closed loop, the exoskeleton performs positive work during upslope walking and negative work during downslope walking, which correspond to the work done by human reported in [46]. With our prior experimental results on potential energy shaping [25] across different tasks, we can safely assume that the proposed approach can provide task-invariant assistance for human subjects.

6) Comparison with the Finite State Machine Approach

In this section, we compared performance of the proposed energy shaping strategies with a classical control paradigm for lower-limb exoskeletons, i.e., Finite State Machine (FSM) structure with Proportional-Derivative (PD) controllers as presented in [3]. In [3], the gait cycle is divided into different phases (i.e., states), and these states employ PD controllers with different sets of proportional and derivative gains. We adopted this structure and the associated parameters in [3] and implemented them on our full biped model for simulations.

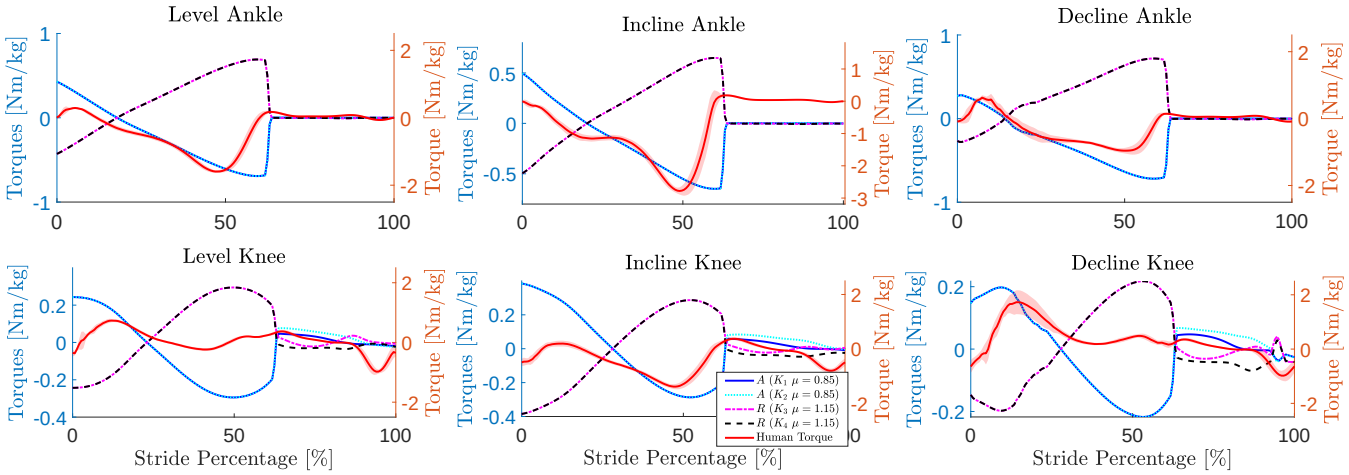

FIGURE 8. Assistive and resistive exoskeleton torques calculated using kinematic data of able-bodied human subjects from [45] walking at $1.2\ \mathrm{m/s}$. All the figures share the same legend and axis. From left to right: the torques acting on ankle and knee joints based on level ground (0°), incline (10°), and decline (-10°). The red solid lines represent the averaged human torques with variance. Positive values represent ankle dorsiflexion and knee extension torques.

Because our full biped model only has an instantaneous double support phase, we removed the double support state and its associated control actions in [3] to conduct simulations, where the simulated torques of the FSM structure are shown in Fig. 9.

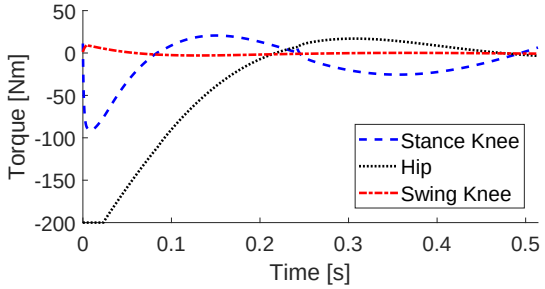

FIGURE 9. FSM torques during one steady step. Directions of torque align with the ones in Fig. 7.

We plotted phase portraits and estimated metabolic costs with both the proposed assistive energy shaping strategies and the FSM control paradigm in Figs. 10 and 11, respectively. To ensure a fair comparison, we set ankle torques of the energy shaping strategies to be zero, as the FSM paradigm presented in [3] only considers actuation at hip and knee joints. From Fig. 10, we can see that the phase portraits rendered by assistive energy shaping strategies were largely contained in the FSM phase portraits, i.e., the energy shaping strategies rendered greater changes in both angular positions and velocities, which indicates the assistive energy shaping strategies outperformed the FSM paradigm in terms of altering human users' joint kinematics. From Fig. 11, we can see that even though ankle torques of the assistive energy shaping strategies were set to zero, the remaining knee and hip torques still managed to reduce the metabolic cost. The FSM control paradigm, on the contrary, increased the metabolic cost compared to the passive gait. It is worth noting that the FSM control paradigm proposed in [3] was originally designed to track reference trajectories instead of augmenting volitional human motion. Nevertheless, results in Fig. 11 indicate that this kinematic based control method does not help improve energy expenditure during simulated walking.

VI. LIMITATION OF THE STUDY

The assistive strategies defined in this paper aim to compensate for the human-exoskeleton system's gravitational forces and inertial terms in the mass matrix, which is not always beneficial during the entire gait cycle. For example, the center of mass of the subject's lower extremities is ahead of the knee joint during late stance. In order to reduce torques exerted by gravitational forces during this phase, the proposed assistive strategies generated flexion torque, which is counterproductive as shown in Fig. 8. Adding virtual weight and inertia during this phase enables the exoskeleton to provide knee extension torque, which can help swing the subject's limb upward. We can improve the current proposed strategies by customizing shaping parameters through online optimization. By relaxing the constraints that assistive parameters (i.e., k_i and μ) need to be less than one, these optimization procedures can find the corresponding optimal strategies during different phases to produce the best gait benefits [47].

In this paper, we assume the upper-body mass of the biped is lumped at the hip joint. This portion of the biped's mass plays a dominant role in deciding the positive definiteness of the mass matrix, therefore it is very difficult to reduce (i.e., compensate for) them given the proposed definition of $\tilde{M}$ while maintaining its positive definiteness. For the particular biped model used in this paper, the shaping parameters k_1 and k_2 must equal to 1 as the hip mass appears in layers of the mass matrix that correspond to these two parameters. Finding complete solutions of the matching conditions and alternative ways to define $\tilde{M}$ can grant us more flexibility in compensating for hip and upper-body masses while ensuring

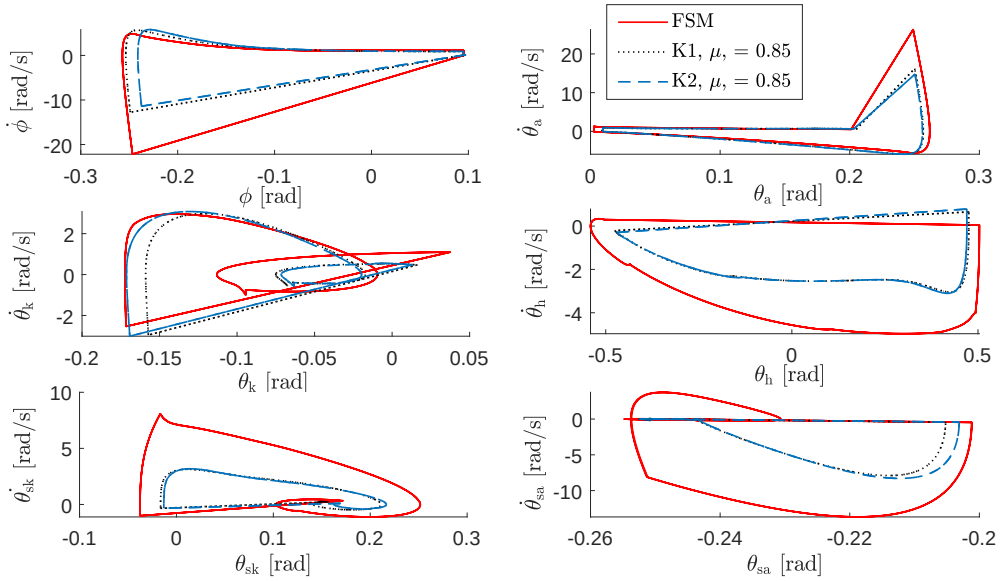

FIGURE 10. Comparison for the phase portraits with FSM and assistive energy shaping strategies. Assistive strategies with parameter sets "$A(K_1,\ \mu = 0.85)$" and "$A(K_2,\ \mu = 0.85)$" were selected to render the phase portraits. For a fair comparison we set ankle torques of the energy shaping strategies to be zero.

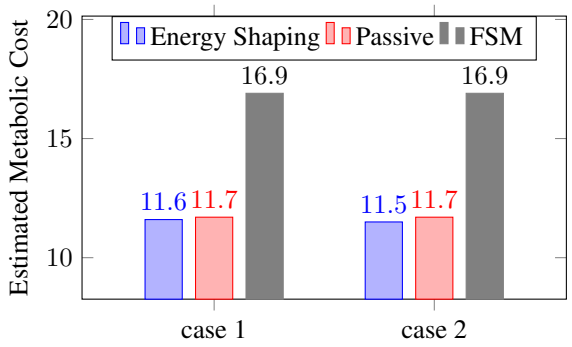

FIGURE 11. Estimated metabolic costs comparison between assistive energy shaping strategies and the FSM control paradigm. Kinetic energy shaping parameter K_i was used in case i, and potential energy shaping parameter $\mu = 0.85$ was used for both cases. We set the ankle torques of energy shaping strategies to zero for a fair comparison.

its positive definiteness.

The proposed control scheme requires knowledge of the subject's limb inertial parameters as well as the exoskeleton's link parameters. The latter can be easily acquired via Solidworks, while the former can be estimated following the method introduced in [38], i.e., estimating the limb's inertial parameters in proportion to the overall body mass, or through system identification by conducting the series of experiments presented in [48]. Model uncertainties and parametric errors may result in torques with different magnitudes, but they can still be assistive or resistive as intended. Large model uncertainties can also damage the passive relationship from human torque input to joint velocity. However, with minor uncertainties, we may be able to show that passivity still exists between the human input and joint velocity but with a different storage function. The effects of model uncertainties on passivity and control performance will be further investigated in future studies.

Finally, we understand the necessity and importance of including experimental results in an exoskeleton-related research paper. However, there are currently no highly-backdrivable, commercialized powered hip-knee-ankle exoskeletons available for sale on the market. This fact makes it almost impossible for us to implement the proposed strategies on a physical exoskeleton to conduct experiments on human subjects. We will further verify our results via experiments in the future once such devices become accessible.

VII. CONCLUSION

In this paper, we generalized our prior work in underactuated total energy shaping to shape both the mass and lower-limb inertia in the actuated part of the mass matrix. We proposed a novel way to define the closed-loop mass matrix with reduced inertial parameters by respecting its inherent structure meanwhile ensuring its positive definiteness. With positive-definite mass matrix in the closed loop, we established passivity from human inputs to joint velocities with total closed-loop energy as the storage function. Based on two common assumptions on human input, we showed Lyapunov stability results for the human-exoskeleton system in the closed loop. Simulation results show that the proposed energy shaping strategies assisted (or resisted) the biped during walking by reducing (or increasing) the magnitude of human torque profiles and metabolic cost. In addition, the proposed assistive strategies outperformed the classical FSM control paradigm in altering joint kinematics and reducing metabolic costs during walking. We further verified the proposed approach by studying exoskeleton torques with able-bodied subject's kinematic data. Future work includes refining this control philosophy to explore the optimal strategies for reducing metabolic cost [47] and studying clinical outcomes

for different patient populations with the powered knee-ankle exoskeleton presented in [42].

REFERENCES

[1] G. Zeilig, H. Weingarden, M. Zwecker, I. Dudkiewicz, A. Bloch, and A. Esquenazi, "Safety and tolerance of the ReWalk™ exoskeleton suit for ambulation by people with complete spinal cord injury: A pilot study," The Journal of Spinal Cord Medicine, vol. 35, no. 2, pp. 96–101, 2012.

[2] S. A. Kolakowsky-Hayner, J. Crew, S. Moran, and A. Shah, "Safety and feasibility of using the Ekso™ Bionic exoskeleton to aid ambulation after spinal cord injury," J Spine, vol. 4, p. 003, 2013.

[3] D. Sanz-Merodio, M. Cestari, J. C. Arevalo, and E. Garcia, "Control motion approach of a lower limb orthosis to reduce energy consumption," International journal of advanced robotic systems, vol. 9, no. 6, p. 232, 2012.

[4] M. Hassan, H. Kadone, T. Ueno, Y. Hada, Y. Sankai, and K. Suzuki, "Feasibility of synergy-based exoskeleton robot control in hemiplegia," IEEE Transactions on Neural Systems and Rehabilitation Engineering, vol. 26, no. 6, pp. 1233–1242, 2018.

[5] A. Ekelem, G. Bastas, C. M. Durrough, and M. Goldfarb, "Variable geometry stair ascent and descent controller for a powered lower limb exoskeleton," Journal of Medical Devices, vol. 12, no. 3, 2018.

[6] T. Yan, M. Cempini, C. M. Oddo, and N. Vitiello, "Review of assistive strategies in powered lower-limb orthoses and exoskeletons," Rob. Auton. Syst, vol. 64, pp. 120–136, 2015.

[7] D. Quintero, D. J. Villarreal, D. J. Lambert, S. Kapp, and R. D. Gregg, "Continuous-phase control of a powered knee–ankle prosthesis: Amputee experiments across speeds and inclines," IEEE Trans. Rob., vol. 34, no. 3, pp. 686–701, 2018.

[8] B. He, G. C. Thomas, N. Paine, and L. Sentis, "Modeling and loop shaping of single-joint amplification exoskeleton with contact sensing and series elastic actuation," in 2019 American Control Conference (ACC). IEEE, 2019, pp. 4580–4587.

[9] S. Chen, Z. Chen, B. Yao, X. Zhu, S. Zhu, Q. Wang, and Y. Song, "Adaptive robust cascade force control of 1-dof hydraulic exoskeleton for human performance augmentation," IEEE/ASME Transactions on Mechatronics, vol. 22, no. 2, pp. 589–600, 2016.

[10] U. Nagarajan, G. Aguirre-Ollinger, and A. Goswami, "Integral admittance shaping: A unified framework for active exoskeleton control," Rob. Auton. Syst., vol. 75, pp. 310–324, 2016.

[11] S. A. Murray, K. H. Ha, C. Hartigan, and M. Goldfarb, "An assistive control approach for a lower-limb exoskeleton to facilitate recovery of walking following stroke," IEEE Transactions on Neural Systems and Rehabilitation Engineering, vol. 23, no. 3, pp. 441–449, 2014.

[12] G. Aguirre-Ollinger, J. E. Colgate, M. A. Peshkin, and A. Goswami, "Inertia compensation control of a one-degree-of-freedom exoskeleton for lower-limb assistance: Initial experiments," IEEE Trans. Neural Syst. Rehabil. Eng., vol. 20, no. 1, pp. 68–77, 2012.

[13] Z. Li, W. Zuo, and S. Li, "Zeroing dynamics method for motion control of industrial upper-limb exoskeleton system with minimal potential energy modulation," Measurement, p. 107964, 2020.

[14] S. H. Collins, M. B. Wiggin, and G. S. Sawicki, "Reducing the energy cost of human walking using an unpowered exoskeleton," Nature, vol. 522, no. 7555, pp. 212–215, 2015.

[15] R. Nasiri, A. Ahmadi, and M. N. Ahmadabadi, "Reducing the energy cost of human running using an unpowered exoskeleton," IEEE Transactions on Neural Systems and Rehabilitation Engineering, vol. 26, no. 10, pp. 2026–2032, 2018.

[16] R. Ortega, J. A. L. Perez, P. J. Nicklasson, and H. J. Sira-Ramirez, Passivity-based control of Euler-Lagrange systems: mechanical, electrical and electromechanical applications. Springer Science & Business Media, 2013.

[17] M. W. Spong, "The passivity paradigm in bipedal locomotion," in Proceedings of the International Conference on Climbing and Walking Robots, Madrid, Spain, 2004.

[18] J. K. Holm and M. W. Spong, "Kinetic energy shaping for gait regulation of underactuated bipeds," Proc. IEEE Int. Conf. Control Appl., pp. 1232–1238, 2008.

[19] R. D. Gregg and M. W. Spong, "Reduction-based control of three-dimensional bipedal walking robots," Int. J. Rob. Res., vol. 29, no. 6, pp. 680–702, 2010.

[20] A. M. Bloch, N. E. Leonard, and J. E. Marsden, "Controlled Lagrangians and the stabilization of mechanical systems. I. the first matching theorem," IEEE Trans. Autom. Control, vol. 45, no. 12, pp. 2253–2270, 2000.

[21] G. Viola, R. Ortega, R. Banavar, J. Á. Acosta, and A. Astolfi, "Total energy shaping control of mechanical systems: simplifying the matching equations via coordinate changes," IEEE Transactions on Automatic Control, vol. 52, no. 6, pp. 1093–1099, 2007.

[22] P. S. Gandhi, P. Borja, and R. Ortega, "Energy shaping control of an inverted flexible pendulum fixed to a cart," Control Engineering Practice, vol. 56, pp. 27–36, 2016.

[23] M. W. Spong, "Energy based control of a class of underactuated mechanical systems," IFAC Proceedings Volumes, vol. 29, no. 1, pp. 2828–2832, 1996.

[24] G. Lv and R. D. Gregg, "Underactuated potential energy shaping with contact constraints: Application to a powered knee-ankle orthosis," IEEE Trans. Control Syst. Technol., vol. 26, no. 1, pp. 181–193, 2018.

[25] G. Lv, H. Zhu, and R. D. Gregg, "On the design and control of highly backdrivable lower-limb exoskeletons: A discussion of past and ongoing work," IEEE Control Syst. Mag., vol. 38, no. 6, pp. 88–113, 2018.

[26] M. Q. Liu, F. C. Anderson, M. G. Pandy, and S. L. Delp, "Muscles that support the body also modulate forward progression during walking," Journal of biomechanics, vol. 39, no. 14, pp. 2623–2630, 2006.

[27] C. L. Dembia, A. Silder, T. K. Uchida, J. L. Hicks, and S. L. Delp, "Simulating ideal assistive devices to reduce the metabolic cost of walking with heavy loads," PloS one, vol. 12, no. 7, p. e0180320, 2017.

[28] R. M. Murray, Z. Li, and S. S. Sastry, A Mathematical Introduction to Robotic Manipulation. CRC press, 1994.

[29] G. Blankenstein, R. Ortega, and A. J. Van Der Schaft, "The matching conditions of controlled Lagrangians and IDA-passivity based control," Int. J. Control, vol. 75, no. 9, pp. 645–665, 2002.

[30] M. W. Spong, S. Hutchinson, and M. Vidyasagar, Robot Modeling and Control. John Wiley & Sons, 2020.

[31] T. Flash and N. Hogan, "The coordination of arm movements: An experimentally confirmed mathematical model," J. Neurosci., vol. 5, no. 7, pp. 1688–1703, 1985.

[32] H. K. Khalil, Nonlinear Systems, 3rd ed. Upper Saddle River, NJ: Prentice Hall, 2002.

[33] J. Lin, N. Divekar, G. Lv, and R. Gregg, "Energy shaping control with virtual spring and damper for powered exoskeletons," in Proceedings of the IEEE Conference on Decision & Control, 2019.

[34] E. Burdet, R. Osu, D. W. Franklin, T. E. Milner, and M. Kawato, "The central nervous system stabilizes unstable dynamics by learning optimal impedance," Nature, vol. 414, no. 6862, pp. 446–449, 2001.

[35] R. Sepulchre, M. Jankovic, and P. V. Kokotovic, Constructive Nonlinear Control. Springer Science & Business Media, 2012.

[36] D. J. Braun, J. E. Mitchell, and M. Goldfarb, "Actuated dynamic walking in a seven-link biped robot," IEEE/ASME Trans. Mechatron., vol. 17, no. 1, pp. 147–156, 2012.

[37] E. R. Westervelt, J. W. Grizzle, C. Chevallereau, J. H. Choi, and B. Morris, Feedback control of dynamic bipedal robot locomotion. CRC press, 2018.

[38] D. A. Winter, Biomechanics and Motor Control of Human Movement. John Wiley & Sons, 2009.

[39] E. P. Washabaugh, T. E. Augenstein, and C. Krishnan, "Functional resistance training during walking: Mode of application differentially affects gait biomechanics and muscle activation patterns," Gait & Posture, vol. 75, pp. 129–136, 2020.

[40] Y. S. Song, S. Ha, H. Hsu, L. H. Ting, and C. K. Liu, "Stair negotiation made easier using novel interactive energy-recycling assistive stairs," Plos one, vol. 12, no. 7, p. e0179637, 2017.

[41] L. Xie, G. Huang, L. Huang, S. Cai, and X. Li, "An unpowered flexible lower limb exoskeleton: Walking assisting and energy harvesting," IEEE/ASME Transactions on Mechatronics, vol. 24, no. 5, pp. 2236–2247, 2019.

[42] H. Zhu, J. Doan, C. Stence, G. Lv, T. Elery, and R. Gregg, "Design and validation of a torque dense, highly backdrivable powered knee-ankle orthosis," in International Conference on Robotics and Automation. IEEE, 2017, pp. 504–510.

[43] A. Silder, T. Besier, and S. L. Delp, "Predicting the metabolic cost of incline walking from muscle activity and walking mechanics," J. Biomech., vol. 45, no. 10, pp. 1842–1849, 2012.

[44] A. Martin and J. Schmiedeler, "Predicting human walking gaits with a simple planar model," J. Biomech., vol. 47, no. 6, pp. 1416–1421, 2014.

[45] K. R. Embry, D. J. Villarreal, R. L. Macaluso, and R. D. Gregg, "Modeling the kinematics of human locomotion over continuously varying speeds and inclines," IEEE Trans. Neural Syst. Rehabil. Eng., vol. 26, no. 12, pp. 2342–2350, 2018.
[46] Q. Li, V. Naing, J. A. Hoffer, D. J. Weber, A. D. Kuo, and J. M. Donelan, "Biomechanical energy harvesting: Apparatus and method," in Robotics and Automation, 2008. ICRA 2008. IEEE International Conference on. IEEE, 2008, pp. 3672–3677.
[47] G. Lv, H. Xing, J. Lin, R. D. Gregg, and C. G. Atkeson, "A task-invariant learning framework of lower-limb exoskeletons for assisting human locomotion," in American Control Conference. IEEE, 2020, pp. 569–576.
[48] R. Mallat, V. Bonnet, W. Huo, P. Karasinski, Y. Amirat, M. Khalil, and S. Mohammed, "Human-exoskeleton system dynamics identification using affordable sensors," in International Conference on Robotics & Automation. IEEE, 2018, pp. 6759–6765.

GE LV (S'15-M'18) received the B.S. (2011) degree in automation and the M.S. (2013) degree in control theory and control engineering from Northeastern University, Shenyang, China. He received the Ph.D. (2018) degree in electrical engineering from the University of Texas at Dallas.

He is an Assistant Professor in the Department of Mechanical Engineering at Clemson University. Prior to joining Clemson in Spring 2020, he was a Postdoctoral Fellow in the Robotics Institute at Carnegie Mellon University. His research is in the control and learning of bipedal locomotion with applications to lower-limb wearable robots. He received the Best Student Paper Award of the 2015 IEEE Conference on Decision and Control.

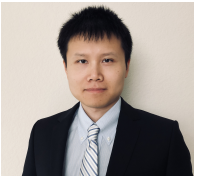

JIANPING LIN (S'19) received the B.S. degree (2012) in applied mathematics from East China Normal University, Shanghai, China. He received the M.S. (2015) degree in mechanical engineering from the University of Texas at Dallas. He is currently pursuing a Ph.D. degree in Robotics Institute, University of Michigan. His research is in the control of bipedal locomotion with applications to powered exoskeletons.

ROBERT D. GREGG (S'08-M'10-SM'16) received the B.S. degree (2006) in electrical engineering and computer sciences from the University of California, Berkeley and the M.S. (2007) and Ph.D. (2010) degrees in electrical and computer engineering from the University of Illinois at Urbana-Champaign.

He joined the Department of Electrical Engineering and Computer Science and the Robotics Institute at the University of Michigan as an Associate Professor in Fall 2019, and he became the Associate Director of Robotics in Fall 2020. Prior to joining UM, he was an Assistant Professor in the Departments of Bioengineering and Mechanical Engineering at the University of Texas at Dallas. His research is in the control of bipedal locomotion with applications to autonomous and wearable robots.